

Signatures of Gas Flows-I: Connecting the kinematics of the H I circumgalactic medium to galaxy rotation

Hasti Nateghi,^{1,2*} Glenn G. Kacprzak^{1,2}, Nikole M. Nielsen^{1,2,3}, Michael T. Murphy¹, Christopher W. Churchill⁴, Sowgat Muzahid⁵, Sameer^{6,7}, Jane C. Charlton⁶

¹Centre for Astrophysics and Supercomputing, Swinburne University of Technology, Hawthorn, Victoria 3122, Australia

²ARC Centre of Excellence for All Sky Astrophysics in 3 Dimensions (ASTRO 3D), Australia

³Homer L. Dodge Department of Physics and Astronomy, The University of Oklahoma, 440 W. Brooks St., Norman, OK 73019, USA

⁴Department of Astronomy, New Mexico State University, Las Cruces, NM 88003, USA

⁵Inter-University Centre for Astronomy and Astrophysics (IUCAA), Post Bag 4, Ganeshkhind, Pune 411 007, India

⁶Department of Physics and Astronomy, The University of Notre Dame, Notre Dame, IN 46544, USA

⁷Department of Astronomy and Astrophysics, The Pennsylvania State University, State College, PA 16801, USA

Accepted 2024 July 26. Received 2024 July 18; in original form 2023 March 10

ABSTRACT

The CGM hosts many physical processes with different kinematic signatures that affect galaxy evolution. We address the CGM–galaxy kinematic connection by quantifying the fraction of H I that is aligned with galaxy rotation with the equivalent width co-rotation fraction, $f_{EW\text{corot}}$. Using 70 quasar sightlines having *HST*/COS H I absorption ($12 < \log(N(\text{H I})/\text{cm}^{-2}) < 20$) within $5R_{\text{vir}}$ of $z < 0.6$ galaxies we find that $f_{EW\text{corot}}$ increases with increasing H I column density. $f_{EW\text{corot}}$ is flat at ~ 0.6 within R_{vir} and decreases beyond R_{vir} to $f_{EW\text{corot}} \sim 0.35$. $f_{EW\text{corot}}$ also has a flat distribution with azimuthal and inclination angles within R_{vir} , but decreases by a factor of two outside of R_{vir} for minor axis gas and by a factor of two for edge-on galaxies. Inside R_{vir} , co-rotation dominated H I is located within ~ 20 deg of the major and minor axes. We surprisingly find equal amounts of H I absorption consistent with co-rotation along both major and minor axes within R_{vir} . However, this co-rotation disappears along the minor axis beyond R_{vir} , suggesting that if this gas is from outflows, then it is bound to galaxies. $f_{EW\text{corot}}$ is constant over two decades of halo mass, with no decrease for $\log(M_{\text{h}}/M_{\odot}) > 12$ as expected from simulations. Our results suggest that co-rotating gas flows are best found by searching for higher column density gas within R_{vir} and near the major and minor axes.

Key words: galaxies: evolution – galaxies: haloes – quasars: absorption lines

1 INTRODUCTION

Gas accretion through the circumgalactic medium (CGM) plays a major role in the growth and evolution of galaxies. Galaxies hierarchically form and evolve via gas flows onto them, which originates from the cosmic web, tidal streams, galaxy mergers, galactic winds, and fountains. Cosmological simulations predict that accretion occurs via two modes depending on whether the gas is shock heated or not (e.g., Kereš et al. 2005; Dekel & Birnboim 2006; Dekel et al. 2009; Faucher-Giguère & Kereš 2011; Stewart et al. 2011a,b, 2013; van de Voort et al. 2011; Hobbs et al. 2015). Focusing on the cold-mode of accretion, Danovich et al. (2015) used cosmological simulations and showed that the kinematics of galaxy disks are comparable to the spin of dark matter halos regardless of the

gas and dark matter angular momentum histories. Their results are consistent with Stewart et al. (2017) who tested five hydrodynamic codes and concluded that the ubiquitous presence of co-directional, co-planar filamentary accretion, with higher angular momentum than dark matter, can support the Λ CDM prediction in galaxy formation. However, observation of CGM gas accretion is difficult and challenging.

A large number of studies have shown that the vast majority of low ionisation metal-line absorption exhibits co-directional and co-planar accretion kinematics (Steidel et al. 2002; Kacprzak et al. 2010, 2011b; Bouché et al. 2013; Burchett et al. 2013; Jorgenson & Wolfe 2014; Bouché et al. 2016; Ho et al. 2017; Rahmani et al. 2018; Martin et al. 2019; Lopez et al. 2020). In these studies, it was noted that the majority or bulk of the absorption seems to align with the rotation direction of the host galaxy. Steidel et al. (2002) used a corotating thick disk model to confirm an extended rotating

* E-mail: hnateghi@swin.edu.au

disk-like structure with some velocity lag is a plausible explanation for the Mg II kinematics detected in the galaxy halos. Furthermore, these signatures of co-rotation in Mg II absorption were investigated by Kacprzak et al. (2010) and Ho et al. (2017) who also found that the bulk of absorption is consistent with observed galaxy rotation. They inferred that the absorbing gas kinematics is either lagging in rotation or infalling. However in these works, absorption systems were counted as either co-rotating or not, without quantifying how much gas was associated with co-rotation.

For the first time, O VI halo–galaxy relative kinematics was examined by Kacprzak et al. (2019a) who found that despite the Mg II absorption, major axis O VI is not likely related to host galaxies’ rotation. However, they could explain the kinematics of O VI detected along the minor axis as outflows with small opening angles and they concluded that O VI that originates from a diffuse high ionisation phase of CGM is likely not a good kinematic indicator for ongoing processes in the CGM.

Some observations of Mg II absorption have shown a bimodal picture where the majority of CGM gas has been detected along the galaxies’ major and minor axes (Bordoloi et al. 2011; Bouché et al. 2012; Kacprzak et al. 2015; Lan & Mo 2018; Langan et al. 2023). These results have inferred that this gas originates from accretion and outflows, respectively. This is further supported by kinematic studies that show signatures of accreting Mg II gas along the galaxy major axes (Steidel et al. 2002; Ho et al. 2017; Diamond-Stanic et al. 2016; Zabl et al. 2019), and outflowing along their minor axes (e.g. Bouché et al. 2012; Schroetter et al. 2019). However, while O VI is also distributed bimodally along the major and minor axes, kinematic studies of O VI show no strong kinematic correlation or signatures of accretion or outflows (Kacprzak et al. 2015; Nielsen et al. 2017; Kacprzak et al. 2019a; Ng et al. 2019). Kacprzak et al. (2019a) also used simulations to suggest that although gas flows are present, they may be masked by a diffuse O VI component.

Various ions have been used to study the CGM that samples different gas densities and temperatures, however, H I may bridge the gap between the low- and high-ionisation halos studied in previous works. It is well known that H I tracks both the low and high ionisation CGM and can be associated with a variety of environments and gas densities like cosmic web filamentary inflows, galactic feedback, tidal stripping caused by mergers, and surrounding H I clouds. So understanding how the H I is kinematically coupled to the rotation of galaxy disks may provide new insights into ongoing gas processes. Cosmological simulations have shown that the high column density H I gas in the halo is mostly associated with gas flows in and out of the host galaxies (Fumagalli et al. 2011; van de Voort et al. 2012; Suresh et al. 2019). In this paper, we observationally test this scenario and examine whether the gas accretion/outflow is dependent on H I column density.

The kinematic relation between Ly α absorption line and the host galaxy was initially studied by Barcons et al. (1995) who found consistency between the kinematics of stellar disks and the halo of two galaxies at $z = 0.075$ and 0.09 and showed that the Ly α gas corotates with the inner disk of the galaxies. Côté et al. (2005) also studied the kinematics of nine H I halos at large galactocentric distances and found an inconsistency between the lower column density Ly α absorption and disk rotation in three systems that can confirm the expectation of cosmic web origin of the gas.

A recent study by French & Wakker (2020) showed that up to $59\% \pm 5\%$ of Ly α absorbers in their sample have consistent kinematics with their host galaxies. They also found an anti-correlation between the corotation fraction of H I and its projected distance from the host galaxies as well as galaxies’ luminosity and incli-

nation angle. In a step forward in methodology, French & Wakker (2020) decomposed their Ly α absorption into multiple components and counted each component separately in order to measure the co-rotation fraction of Ly α absorption. This better quantified how much gas in each absorption system is consistent with a co-rotation model. However, this approach only works for low column density, unsaturated absorption systems, with no complex velocity structure. When absorption systems have a complex velocity structure or are saturated, then results will be dependent on how many components one fits into the data and the assumptions being made, e.g., assume the H I has the same velocity structure of the metal lines, or use the least amount of fitted components to achieve the best fit, etc. In this study, we have taken a new approach to quantify the amount of gas that has kinematics consistent with co-rotation, which relies on the data rather than user/model absorption decomposition.

Using the quasar absorption line technique, we quantify the kinematic connections between the CGM H I gas and their host galaxies in 70 galaxy-CGM absorption pairs. The high resolution galaxy spectra obtained by the Echelle Spectrograph and Imager (ESI, Sheinis et al. 2002) on Keck II provided us with the rotation curves for most galaxies. We also measured the H I gas properties such as kinematics, equivalent widths, and column densities using the Ly α absorption lines detected in the background quasar spectra observed with the Cosmic Origins Spectrograph (COS) on the *Hubble Space Telescope* (HST). The quasar sightlines in our sample trace H I gas within projected distances of $10 \leq D \leq 815$ kpc of galaxies over the redshift range of $z = 0.002 - 0.55$. Here for the first time, we measure the fraction of H I equivalent width in each system that could be kinematically coupled with the rotation of its host galaxy to avoid any fitting and model dependencies and to provide a better estimate of co-rotating gas around galaxies.

The paper is organized as follows: In Section 2 we describe the data and analysis. This included our new method for quantifying the co-rotation fraction ($f_{EW_{corot}}$). In Section 3 we present the results of how $f_{EW_{corot}}$ varies as a function of the H I column density, impact parameter, virial radius normalised impact parameter, azimuthal angle, galaxy inclination angle, stellar and halo mass. In Section 4 we discuss our results and present our concluding remarks in Section 5. Throughout we adopt an $H_0 = 70 \text{ km s}^{-1} \text{ Mpc}^{-1}$, $\Omega_M = 0.3$, $\Omega_\Lambda = 0.7$ cosmology.

2 OBSERVATIONS AND ANALYSIS

Our sample comprises 70 galaxy–H I absorption pairs that span a redshift range of $z = 0.002 - 0.55$ and within impact parameters of $D = 10 - 815$ kpc. Every galaxy has Ly α absorption detected in HST/COS G130M or G160M quasar spectra with column densities ranging between $\log(N(\text{H I})/\text{cm}^{-2}) = 12.6 - 20.9$. We have obtained the kinematics/rotation curves of 39 galaxies with Keck/ESI, which were observed as part of the Multiphase Galaxy Halos survey (e.g., Kacprzak et al. 2015; Nielsen et al. 2017; Pointon et al. 2019; Nateghi et al. 2021). The remaining 23 galaxy kinematics were obtained from French & Wakker (2020). Four galaxies having multiple quasar sightlines (see Table A1), which result in a total of 62 galaxies for the entire sample and 70 galaxy-absorption pairs. The sample contains a mixture of galaxy-selected (Pointon et al. 2019; French & Wakker 2020) and absorption-selected (Tripp et al. 2008) absorber–galaxy pairs.

We focus on isolated galaxies in order to reduce any environmental effects, such as perturbations on the galaxy rotation curves or gas distributions due to interactions or major mergers which

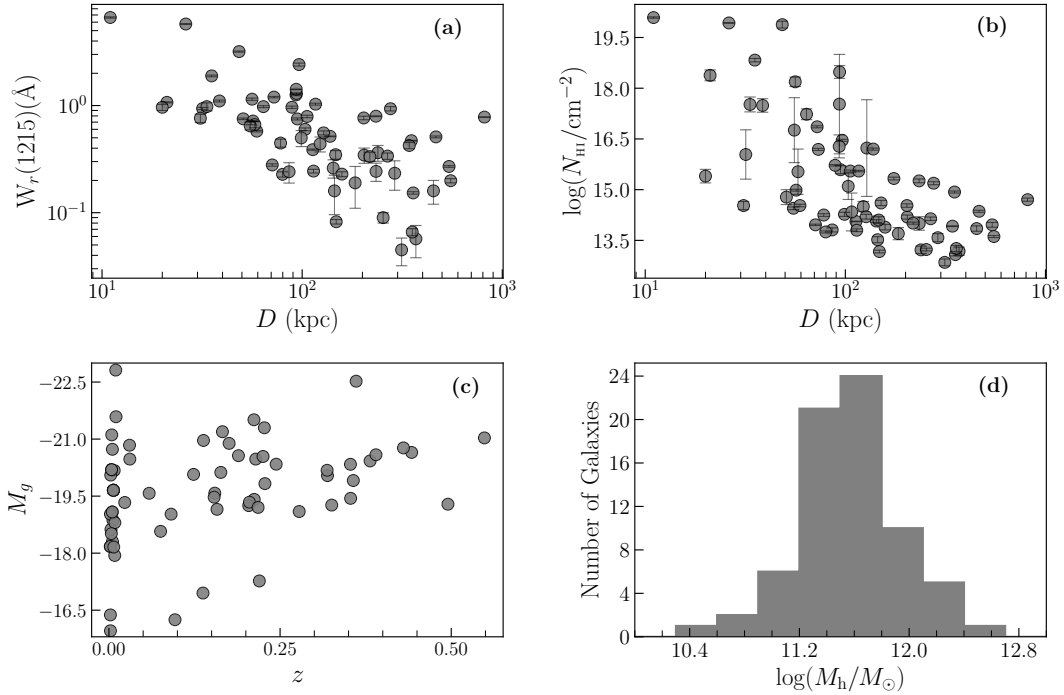


Figure 1. (a) Rest-frame equivalent width of Ly α ($W_r(1215)$) as a function of impact parameter (D). We see a clear anti-correlation between absorption strength and impact parameter, which is consistent with the literature. (b) Distribution of H I absorption column densities in our sample as a function of projected distance from galaxies. (c) The g-band absolute magnitude of galaxies as a function of redshift. (d) The halo mass distribution of the galaxies in our sample.

complicate correlations between galaxy and CGM kinematics (e.g., Pointon et al. 2017; Nielsen et al. 2018, 2022; Fernández-Figueroa et al. 2024). For our higher redshift galaxies selected from Pointon et al. (2019), they report that there are no major companions within 100 kpc and with velocity separations less than 500 km s^{-1} . For the low redshift galaxies selected from French & Wakker (2020), they report that the galaxies are relatively isolated based on their likelihood criteria and within $3 R_{\text{vir}}$ of a background quasar. In both samples, galaxies may still have nearby minor companions, which likely do not affect the kinematics of the larger galaxy. Summaries of the H I observations and galaxy sample are presented in Table B1 and Table A1, respectively. A summary of the sample is also presented in Fig. 1. Fig. 1(a) shows the rest-frame equivalent width of Ly α ($W_r(1215)$) and (b) shows the H I column density ($\log(N(\text{H I})/\text{cm}^{-2})$) as a function of impact parameter (D). These panels show the strong anti-correlation between absorption strength and D . Fig. 1(c) and (d) shows the absolute magnitude and halo mass distributions of our sample, respectively. We describe the details of the data for this sample in the following subsections.

2.1 Galaxy morphologies

In order to connect the CGM absorption to the host galaxies, we need the galaxy morphologies and the alignment of the quasar sightline relative to the galaxy disks (i.e., inclination and azimuthal angles). We obtained previously published inclination angles and azimuthal angles for 23 galaxies (French & Wakker 2020), which are listed in Table A1. We further obtained previously published morphologies/geometries for 28 galaxies (Kacprzak et al. 2015, 2019a,b), which were computed using GIM2D (Simard et al. 2002) models of *HST* images with ACS, WFC3, or WFPC2 in the F702W, F814W, or F625W filters as listed in Table B1. Here we add new models for

5 galaxies having *HST* images and 5 galaxies with Pan-STARRS (hereafter PS; Chambers et al. 2016) images, which are listed in Table B1. The orientation of the galaxies, such as their inclination (i) and azimuthal angle (Φ), were modelled following the methods adopted from Kacprzak et al. (2011a) and Kacprzak et al. (2015). We fit two-component disc+bulge models using GIM2D (Simard et al. 2002) to the *HST* and PS images using modelled point spread functions (see Kacprzak et al. 2015). The galaxy disk component is modelled with an exponential profile and the bulge component has a Sersic profile with $0.2 < n < 4.0$. The modelled inclination and azimuthal angles, and their errors, for all galaxies are listed in Table A1. We adopt the convention of the azimuthal angle $\Phi = 0^\circ$ to be along the galaxy major axis and $\Phi = 90^\circ$ to be along the galaxy minor axis.

Our galaxies have a full range of azimuthal and inclination angles (see Table A1). We test for potential effects of a biased distribution in azimuthal and inclination angle on our results by conducting a one-dimensional Kolmogorov-Smirnov (KS) test on Φ and i distributions. Our analysis indicates that the azimuthal angle is consistent with the expected flat distribution for a random sample of galaxies at a significance level of 1.36σ . We also find that the inclination angles are consistent with the expected $\sin(i)$ distribution for a random sample of galaxies (Law et al. 2009), at the significance level of 1.84σ . Although a preference towards edge-on galaxies is ideal for examining outflows and inflows, we have determined that our results remain unchanged within the errors reported here when we exclude galaxies with $i < 30^\circ$ (14 galaxies in total). Thus, we include all galaxies in our analysis.

2.2 Galaxy photometries and masses

The behaviour of the CGM is dependent on galaxy mass and its properties vary with location within the virial radius of the halo (Chen et al. 2010; Churchill et al. 2013a,b; Tumlinson et al. 2013; Oppenheimer et al. 2016; Ng et al. 2019). Therefore we have computed the stellar masses for all galaxies using the rest-frame $g - r$ colour and g -band mass-to-light ratio (M/L) relation from Bell et al. (2003). Galactic extinction corrections are not applied as they are on the order of the uncertainties in our method. Given the range of redshifts and galaxy angular extents in our sample, we have used a range of catalogues, such as PS, SDSS (York et al. 2000), and DESI Legacy surveys (Dey et al. 2019), to obtain the galaxy photometry and colours.

For galaxies with $z > 0.05$, we obtained g and r Kron magnitudes from PS. In cases where PS photometry was not available, we used either SDSS model magnitudes or *HST* photometry. To apply the M/L ratio relation, the rest-frame colours of galaxies are required. We applied K -corrections following the methods described by Nielsen et al. (2013) to obtain rest-frame absolute g - and r -band magnitudes. For the galaxies with no $g - r$ observed colour, we assumed an Sbc type, which represents the typical galaxy colour found for galaxies associated with CGM absorption. (Steidel et al. 1994; Zibetti et al. 2007; Nielsen et al. 2013; Kacprzak et al. 2015).

Galaxies with $z < 0.05$ have larger angular extents, which typically results in underestimated g -band magnitudes from SDSS and PS. To obtain their g -band absolute magnitudes we adopted the colour transformation from Blanton & Roweis (2007), $g = B - 0.2354 + 0.3915((g - r) - 0.6102)$, to convert B -band magnitudes to g -band magnitudes. The B -band magnitudes are computed using the B -band galaxy luminosity function of Marzke et al. (1994) with the galaxies' luminosities adopted from French & Wakker (2020). The galaxy colours are measured using DESI Legacy Survey imaging in g and r bands. Here, K -corrections are not applied for these low redshift galaxies since they are negligible. The measured $g - r$ colour for all the galaxies is presented in Table A1.

Using our uniformly computed photometry, we show the g -band absolute magnitude distribution of our galaxies as a function of redshift in Fig. 1(c). We find that the vast majority of our galaxies reside above $M_g = -18$ with a few less luminous galaxies. Our sample appears to be mass complete near $M_g = -19$, however this cannot be concluded since this plot is limited to absorbers only and does not account for the H I absorption–mass dependence (Bordoloi et al. 2018). Since this work attempts to eliminate objects with major companions that could have a larger influence on the CGM kinematics, we are less concerned about lower mass companions like LMCs, dwarfs, etc., which can be considered as part of the more massive halo and their kinematics. So having a complete survey to the same depths in each field (i.e., similar central-to-satellite mass ratio limit) is more important than equal mass sensitivity (i.e., $10^9 M_\odot$) across all fields, which permits us to examine lower masses at lower redshifts. We have also verified that our results remain unchanged within the errors reported here when we exclude low luminosity/mass galaxies ($M_g > -19$, 9 galaxies in total). Thus, we include all galaxies in our analysis.

To test the validity of our computed masses, we compared our values with the stellar masses of the 11 galaxies that overlap with the COS-Halos sample (Werk et al. 2013). We found a mean difference of 0.065 dex between the two samples., which provides confidence in our mass estimates.

We also converted the galaxy stellar masses (M_*) to halo

masses (M_h) using the stellar-to-halo mass relation (SHMR) from Girelli et al. (2020). We adopted the parameterised SHMR in two redshift bins of $0.0 \leq z < 0.2$ and $0.2 \leq z < 0.5$. The best-fit parameters with a relative scatter of 0.2 dex from their Table 2 are used for our conversions and uncertainty calculations. The distribution of galaxy masses is shown in Fig. 1. The halo masses have a median value of $\log(M_h/M_\odot) = 11.5$ and span a full range of $10.5 < \log(M_h/M_\odot) < 12.7$. The virial radius of all the galaxies in our sample is calculated following the formalism of Bryan & Norman (1998). The virial radii span a range of $61 < R_{\text{vir}} < 324$ kpc with a median value of $R_{\text{vir}} = 131.5$ kpc. The virial radius normalised impact parameters have a range of $0.1 \leq D/R_{\text{vir}} \leq 5.0$, with a median value of $D/R_{\text{vir}} = 0.91$. The galaxy masses, R_{vir} and D/R_{vir} can be found in Table A1.

2.3 Galaxy spectroscopy and kinematics

To compare the CGM kinematics to the kinematics of the galaxies, we require galaxy redshift zeropoints and their rotation curves. The galaxy kinematics for 23 galaxies were obtained from French & Wakker (2020). We further obtained spectra for 39 galaxies using the Keck/ESI over the course of 10 observing nights across 2010, 2014, 2015, and 2016. The wavelength coverage of ESI is 4000 – 11000 Å, which covers a range of emission lines like the [O II] doublet, H β , the [O III] doublet, H α , and N II doublet. The width of the ESI slit was set to 1'' and it is 20'' long. The slit position angle was selected to be aligned with the optical major axis of each galaxy to acquire their full range of rotation velocities (see Fig. 2). The echellette spectra obtained over 2014 – 2016 were binned on-chip by two in the spatial and spectral directions resulting in a pixel size of 0''.27 – 0''.34 and spectral resolution of $R \sim 4600$ with a sampling rate of 22 km s⁻¹ pixel⁻¹ (FWHM \sim 65 km s⁻¹). The spectra obtained in 2010 were binned only spatially on-chip by two.

The standard echelle package in IRAF was used to combine, to perform flat-field correction, and to extract the ESI spectra. The wavelength solutions were derived using a list of known sky-lines having vacuum wavelengths, where our wavelength solutions have a rms scatter of ~ 0.03 Å or about 2 km s⁻¹. The spectra were also heliocentric velocity corrected.

The galaxy rotation curves were extracted following the method described in Kacprzak et al. (2010) with a similar approach used by Vogt et al. (1996) and Steidel et al. (2002). In summary, we adopted a three-pixel-wide aperture size and shifted the aperture by one pixel intervals along the spatial direction and extracted a series of spectra along the major axis of each galaxy. We performed Gaussian fits to galaxy emission lines (mainly H α and H β), which provided the wavelength centroids used to derive the galaxy systemic redshifts and rotation curves. The galaxy redshifts are listed in Table A1. Fig. 2 shows the extracted rotation curve of a galaxy at $z_{\text{gal}} = 0.20419$ associated with H I absorption in J113910 – 135043, where the H α emission line was used to extract this rotation curve. In this particular geometry, the quasar sightline is positioned in the negative direction along the slit along the galaxy major axis.

2.4 Quasar spectroscopy

Our sample contains 58 quasars, with some quasars probing multiple galaxies and some galaxies having multiple quasar sightlines. The background quasars in each field were observed with the *HST*/COS and Table B1 provides details of the quasar spectroscopy with the coordinates, redshifts, *HST* program IDs, and the COS gratings used.

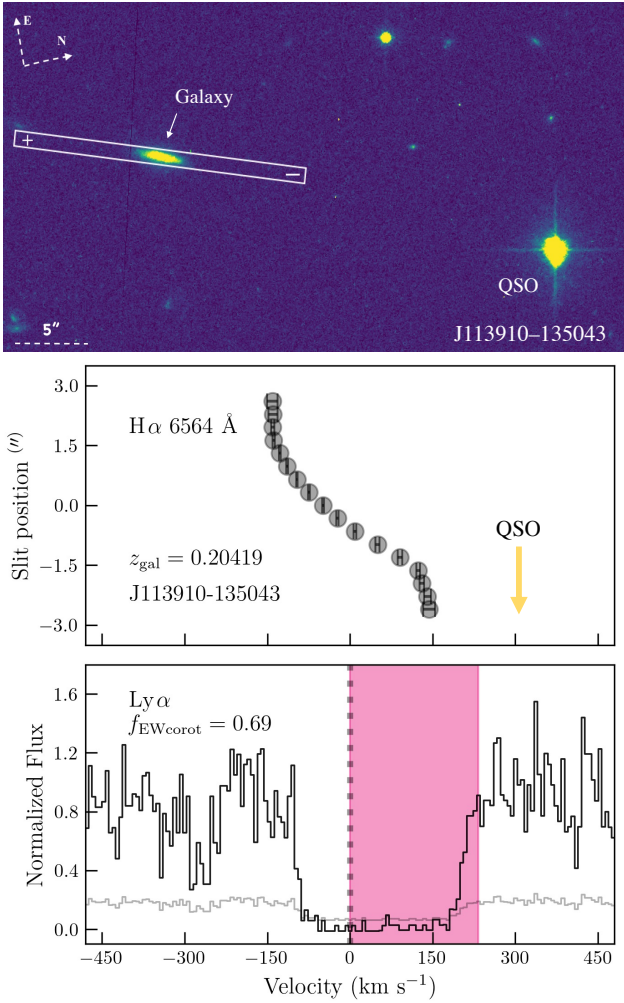


Figure 2. (Top) *HST*/*ACS* image of the quasar field J113910 – 135043 in the F702W filter. The $1'' \times 20''$ Keck/ESI slit is centred on the galaxy and is aligned with the projected major axis, where the “+” and “-” signs indicate the positive and negative slit positions. The quasar (QSO) is located $27.6''$ ($D = 93.2$ kpc and $D/R_{\text{vir}} = 0.62$) away from the galaxy on the negative slit position side. (Middle) Extracted H α rotation curve for the galaxy at $z_{\text{gal}} = 0.20419$. The galaxy velocities are receding in the direction of the quasar sightline, so any co-rotating H I CGM absorption should also have positive velocities. (Bottom) The Ly α absorption profile observed in the background quasar spectrum, where black is the data and grey is the error spectrum. The velocity window of the pink-shaded region is defined to cover the absorption residing to the side of the galaxy systemic velocity (vertical dotted line) corresponding to the galaxy’s rotation curve in the direction of the quasar sightline. We integrate over this region to determine the equivalent width co-rotation fraction, which is $f_{\text{EWcorot}} = 0.69$ for this absorption system.

The far-ultraviolet gratings G130M and/or G160M have a moderate resolving power of $R \sim 20,000$, giving a full width at half maximum of ~ 18 km s⁻¹ and wavelength coverage of 1410 – 1780 Å. We used the STScI CALCOS V2.21 pipeline (Massa & et al. 2013) to reduce and flux calibrate all spectral data acquired from the *HST* archive. All spectra are heliocentric velocity corrected and in vacuum wavelengths. We co-added multiple integrations with the IDL

code COADD_X1D¹ (Danforth et al. 2010) and binned spectrally by three pixels to enable an increased signal-to-noise ratio. Continuum normalisation was performed by fitting low-order polynomials to the spectra while excluding regions with strong absorption lines.

We implemented the interactive SYSANAL code (Churchill 1997; Churchill & Vogt 2001) to define the velocity bounds of Ly α absorption profiles, compute the optical depth-weighted mean systemic redshifts of absorption (z_{abs}), and to compute the rest-frame equivalent widths ($W_r(1215)$). Column densities were adopted from Sameer et al. (2024) and are listed in Table C1. They use a cloud-by-cloud, multi-phase, Bayesian ionisation modelling approach to determine the physical properties of the absorption systems. It has been demonstrated to produce reliable column densities even when a saturated Ly α is the only H I line available (Sameer et al. 2021). We do note however, that our results do not depend on the accuracy of the H I column densities as we have selected our highest data bins to account for saturation of Ly α . Where column densities were not available in the literature, we used VPFIT² (Carswell & Webb 2014) to measure the H I column densities by fitting Voigt profile models to the absorption lines. We used the appropriate line spread function³ at the corresponding lifetime position when fitting the data. The H I column densities for all absorption systems are listed in Table C1.

Fig. 1 shows the distribution of rest-frame equivalent widths and column densities as a function of the impact parameter. Both show a strong anti-correlation between the absorption strength and D . While high column density systems tend to exist only within the inner halos of galaxies, lower column density systems tend to reside at low and high impact parameters.

2.5 H I co-rotation fractions

We developed a new method for measuring the co-rotation fraction of the H I halo. For each Ly α absorption system, we compute the fraction of the total equivalent width that is consistent with our co-rotation model. The only dependent choice required is the velocity window we consider when determining whether the gas is consistent with co-rotation. We choose a velocity window that includes all gas from the systemic velocity onward in the direction of galaxy rotation towards the quasar sightline, defined as f_{EWcorot} . A value of 1 indicates all of the gas is consistent with a co-rotation scenario, while 0 suggests none of the gas is consistent with a co-rotation scenario. Errors on the co-rotation fraction were calculated by bootstrapping the errors associated with galaxy redshift and the absorption profile and range from 0.001 – 0.008.

Fig. 2 (middle) shows the galaxy rotation curve. In this galaxy-quasar pair, the quasar resides on the negative side of the slit position, where the galaxy’s rotation is redshifted with respect to its systemic velocity. For our velocity window criterion, we include all the absorption between the galaxy systemic velocity and the most positive velocity of the absorption boundary defined by SYSANAL as highlighted in pink in Fig. 2 (bottom). In this case, 69% of the absorption equivalent width is consistent with a co-rotation model. This value is comparable to other works where they state that the

¹ <http://casa.colorado.edu/~danforth/science/cos/costools.html>

² <http://www.ast.cam.ac.uk/~rfc/vpfit.html>

³ <https://www.stsci.edu/hst/instrumentation/cos/performance/spectral-resolution>

bulk of the absorption is consistent with co-rotation models (e.g., Ho et al. 2017).

Our new method still allows for a comparison to other works even though different variations of kinematic methods are used (e.g., Steidel et al. 2002; Kacprzak et al. 2010; Ho et al. 2017; Kacprzak et al. 2019a; French & Wakker 2020) since they discuss co-rotation in a binary form and only when the majority/bulk of the gas is consistent with the model is it co-rotating. Here, we can state that the bulk of the absorption is co-rotating when $f_{\text{EWcorot}} \geq 0.5$. Our result now provides a quantification of the amount of gas that is consistent with a co-rotation model. However, we do note that the f_{EWcorot} should be considered an upper limit, and it is plausible that the true co-rotation fraction could be lower since there is the possibility of selecting gas at higher velocities than the galaxy maximum rotation velocity.

3 DEPENDENCE OF H I CO-ROTATION WITH GALAXY PROPERTIES

We investigate the kinematic connection between galaxies and their surrounding H I halos to test the scenarios of gas co-rotation and/or accretion through the CGM. For this purpose, we used the galaxies' rotation curves and velocities of the Ly α absorption along quasar sightlines. We remind the reader that although a preference towards edge-on galaxies is ideal for examining outflows and inflows, we determined that our results remain unchanged within the errors reported here when we exclude galaxies with $i < 30$ deg. Thus, for the remainder of the paper, we include all galaxies in our analysis. In the following sections, we explore the Ly α equivalent width co-rotation fractions, f_{EWcorot} , for a range of properties such as absorption strength, impact parameter, galaxy orientation, and stellar mass.

3.1 f_{EWcorot} and H I column density

Simulations show that the CGM has a vast range of H I column densities and that different column density regimes may probe different components of the CGM (Fumagalli et al. 2011; Suresh et al. 2019). For example, simulations have shown that Lyman Limit Systems (LLSs) may be the best probe of CGM gas flows, including accretion and outflows (van de Voort et al. 2012; Faucher-Giguère & Kereš 2011; Faucher-Giguère et al. 2015; Hafen et al. 2017). Here we explore how the gas co-rotation fraction of Ly α behaves as a function of H I column density.

Figure 3 presents f_{EWcorot} as a function of H I column density. The grey data points are individual absorption system column densities. We find that the low column density systems span the full range of f_{EWcorot} whereas higher column density systems, particularly those above $\log(N(\text{H I})/\text{cm}^{-2}) \sim 16$ tend toward higher f_{EWcorot} . To better investigate this trend, we divided the data into three bins of column density: $\log(N(\text{H I})/\text{cm}^{-2}) < 14.5$, $14.5 \leq \log(N(\text{H I})/\text{cm}^{-2}) < 16.2$, and $\log(N(\text{H I})/\text{cm}^{-2}) \geq 16.2$. The large pink squares represent the mean f_{EWcorot} in each column density bin where the vertical error bars are calculated using 10,000 bootstrapped realisations of the data and their errors to measure the mean and its 1σ error. We find that the f_{EWcorot} is correlated with $\log(N(\text{H I})/\text{cm}^{-2})$, where the co-rotation fraction increases from 0.42 ± 0.06 for the lowest column density bin to 0.59 ± 0.05 in the highest column density bin. Therefore stronger absorbers are more likely to have kinematics that are consistent with having gas with

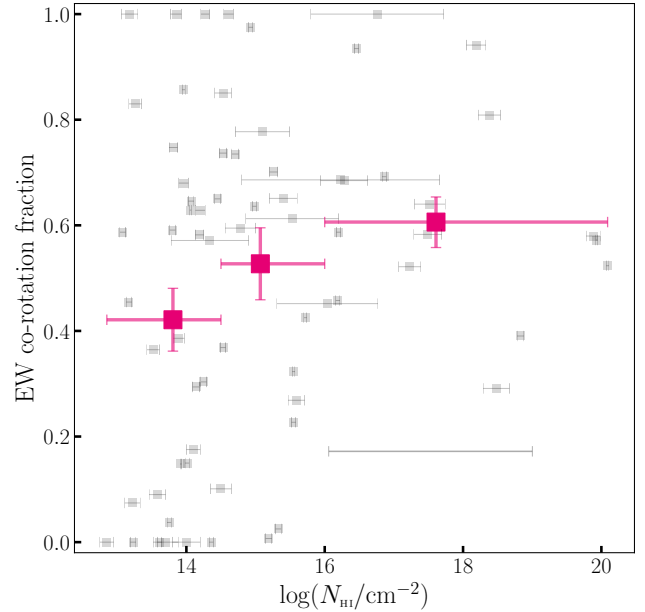


Figure 3. Equivalent width co-rotation fraction (f_{EWcorot}) as a function of H I column density. The grey data points are individual galaxies and the grey bars represent the column density errors. The horizontal grey bar spanning $16 \leq \log(N(\text{H I})/\text{cm}^{-2}) \leq 19$ at $f_{\text{EWcorot}} \sim 0.2$ represents an absorption system where the column density is poorly constrained due to saturation. The pink squares are the averaged f_{EWcorot} in bins of column density, where the error bars represent the column density ranges of each bin and the 1σ bootstrapped errors on f_{EWcorot} . The fraction of H I absorption that is consistent with co-rotation increases with increasing the column density.

line of sight velocities aligned with the rotation curve of the galaxy, increasing from 40% to 60% co-rotation.

3.2 f_{EWcorot} vs D and D/R_{vir}

Quasar absorption line studies have shown that H I column densities decrease with increasing impact parameter (e.g., Tumlinson et al. 2013; Borthakur et al. 2015; Kacprzak et al. 2021). Combined with our previous results showing the co-rotation fraction may also be dependent on column density, we explore how it behaves as a function of impact parameter as well as column density. To do this, we bifurcated our sample into two sub-samples with splits at $\log(N(\text{H I})/\text{cm}^{-2}) = 14.5$ and $\log(N(\text{H I})/\text{cm}^{-2}) = 16.2$. A column density of 14.5 appears to be where the transition occurs between the CGM and IGM (e.g., Rudie et al. 2012; Wakker et al. 2015; Bouma et al. 2021) and so significant differences in the co-rotation fraction above and below this value can indicate whether the galaxy influences its surroundings beyond R_{vir} . The higher column density cut at 16.2 was selected since this is the lower limit for partial Lyman limit systems (pLLs) following the classification by Lehner et al. (2018), which is where a bimodality in CGM metallicity is the most apparent (Lehner et al. 2013; Wotta et al. 2016) and where simulations suggest that signatures of gas flows may become dominant.

Figure 4(a) shows the first-order polynomial fits to f_{EWcorot} as a function of impact parameter for absorption systems bifurcated by $\log(N(\text{H I})/\text{cm}^{-2}) = 14.5$. The dark and light purple fits present the low (dashed line) and high (dotted line) column density system subsamples, respectively. The 1σ error on the fits is measured by bootstrapping the fit and calculating the average and standard de-

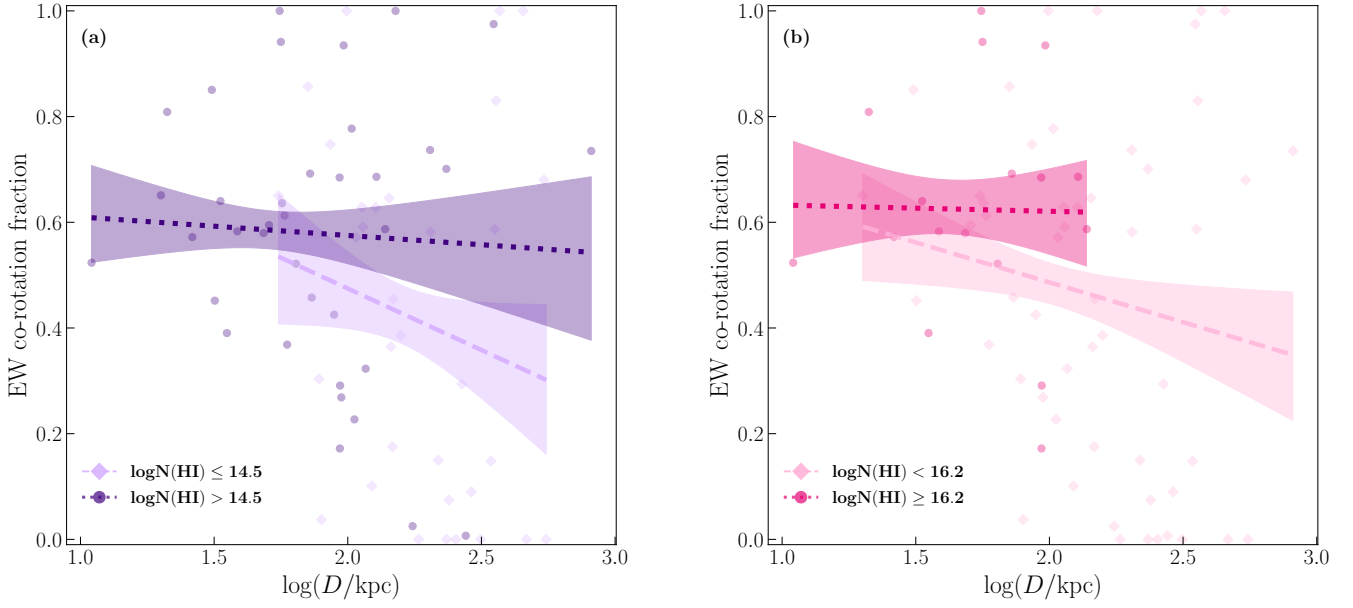


Figure 4. Equivalent width co-rotation fraction ($f_{EWcorot}$) as a function of impact parameter (D). (a) The sample is split into low ($\log(N(\text{HI})/\text{cm}^{-2}) \leq 14.5$) and high ($\log(N(\text{HI})/\text{cm}^{-2}) > 14.5$) column density. The slope of the dark purple fit (high column density subsample) is consistent with the light purple fit (low column density systems) within the 1σ bootstrap errors. (b) The sample is divided into low ($\log(N(\text{HI})/\text{cm}^{-2}) < 16.2$) and high ($\log(N(\text{HI})/\text{cm}^{-2}) \geq 16.2$) column density absorbers. While $f_{EWcorot}$ is consistent with having a flat distribution with D for all subsamples, the lower column density subsamples tend towards a decreasing $f_{EWcorot}$ as the impact parameter increases.

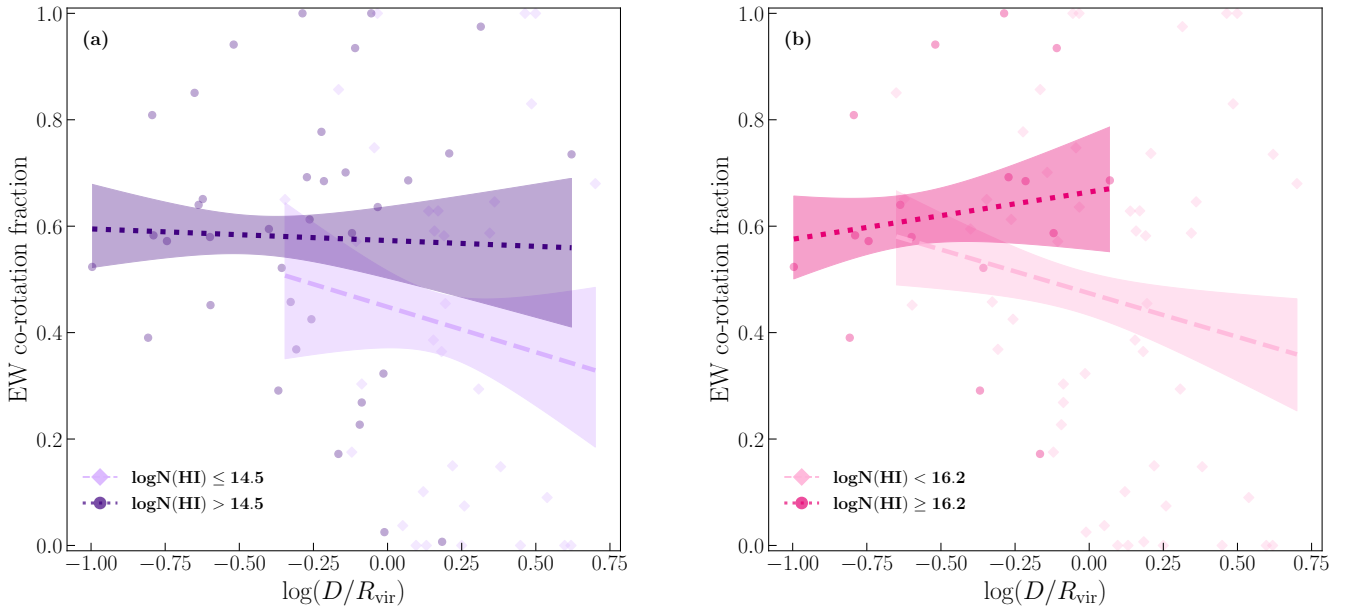


Figure 5. Same as Fig. 4 except the equivalent width co-rotation fraction ($f_{EWcorot}$) is a function of D/R_{vir} . (a) For high column density systems (dotted dark purple), the $f_{EWcorot}$ vs $\log(D/R_{vir})$ can be explained with an almost flat distribution. However, the low column density systems (dashed light purple) are decreasing with increasing D/R_{vir} . (b) For high column density systems (dotted dark pink), the $f_{EWcorot}$ vs $\log(D/R_{vir})$ can be explained with a slightly increasing distribution, although the curve is still consistent with being flat. The $f_{EWcorot}$ of low column density systems (dashed light pink) decreases with increasing D/R_{vir} . Compared to Fig. 4, normalising by R_{vir} affects the slope, where the co-rotation fraction of low column density subsamples decreases with distance more quickly and significantly. This suggests that the mass of the galaxy plays a role in determining whether the gas is co-rotating with the galaxy at a given location.

viation of 10,000 realisations of the data and their errors. We find that the f_{EWcorot} for lower column density systems, which reside at larger impact parameters and are more IGM-like, appear to be decreasing but the error bars in the slope are consistent with a flat distribution ($f_{\text{EWcorot}} = (-0.17 \pm 0.26) \log(D/\text{kpc}) + (0.80 \pm 0.58)$). Higher column density systems, which span a large range of impact parameters, also have a distribution that is consistent with being flat ($f_{\text{EWcorot}} = (-0.04 \pm 0.13) \log(D/\text{kpc}) + (0.65 \pm 0.22)$).

Fig. 4(b) shows the first-order polynomial fits to f_{EWcorot} for absorption systems bifurcated by $\log(N(\text{H I})/\text{cm}^{-2}) = 16.2$. The light and dark pink fits represent low (dashed line) and high (dotted lines) column densities, respectively. The 1σ errors are also measured with the bootstrapping method. We see that the larger column density systems reside within 100 kpc, while the lower column density systems extend to larger impact parameters. We find that the statistical behaviour of low column density ($f_{\text{EWcorot}} = (-0.11 \pm 0.13) \log(D/\text{kpc}) + (0.72 \pm 0.27)$), and high column density ($f_{\text{EWcorot}} = (-0.01 \pm 0.16) \log(D/\text{kpc}) + (0.64 \pm 0.27)$) systems are not significantly different, aside from their extent. The trend in low column density systems (light pink dashed line) shows a slightly decreasing f_{EWcorot} with increasing impact parameter, yet it is consistent with a flat distribution. The high column density systems remain roughly constant with impact parameter (dark pink dotted line).

These trends, or lack thereof, should be taken with caution given that our sample covers a wide range of galaxy masses across 2.5 dex (Fig. 1). In fact, the CGM seems to be self-similar over a large mass range (Churchill et al. 2013a,b), where more massive galaxies host CGM gas out to larger distances, but similar absorption strengths are found at similar fractions of the virial radius across the mass range. Therefore, we normalise the impact parameter by the galaxy virial radius and present the computed values of D/R_{vir} in Table A1.

We investigate this mass dependence in Fig. 5(a), which presents the f_{EWcorot} (purple) versus D/R_{vir} for absorption systems split at a column density of $\log(N(\text{H I})/\text{cm}^{-2}) = 14.5$. We find that higher column density systems (dark purple dotted line) have a flat distribution ($f_{\text{EWcorot}} = (-0.02 \pm 0.13) \log(D/R_{\text{vir}}) + (0.57 \pm 0.07)$) that extends beyond the virial radius of the galaxies. For the lower column density systems (light purple dashed line), we find a slightly decreasing trend ($f_{\text{EWcorot}} = (-0.20 \pm 0.26) \log(D/R_{\text{vir}}) + (0.45 \pm 0.07)$) where the f_{EWcorot} could decrease beyond the virial radius. Overall, both low and high column density systems are roughly consistent with each other over the overlapping D/R_{vir} range.

In Fig. 5(b) high column density systems with $\log(N(\text{H I})/\text{cm}^{-2}) \geq 16.2$ are fitted with a first-order polynomial (dotted dark pink line) that has a positive slope ($f_{\text{EWcorot}} = (0.10 \pm 0.16) \log(D/R_{\text{vir}}) + (0.66 \pm 0.11)$), yet is still consistent with a flat distribution. We find a slightly decreasing trend for the low column density systems with $\log(N(\text{H I})/\text{cm}^{-2}) < 16.2$ plotted as a dashed light pink line ($f_{\text{EWcorot}} = (-0.16 \pm 0.13) \log(D/R_{\text{vir}}) + (0.47 \pm 0.04)$), showing that the f_{EWcorot} decreases for absorption detected mostly beyond the virial radius of galaxies. This indicates that f_{EWcorot} anti-correlates with impact parameter for low column density absorbers and is flat for high column density systems.

The low significance of these (anti-)correlations could be improved by increasing the sample size. Nevertheless, it seems likely that normalising by the virial radius is an important step in understanding how the gas behaves within galaxy haloes. Regardless of the column density cut selected, a large fraction of the gas ($\sim 60\%$) has kinematics consistent with co-rotation within the virial radius.

Outside of the virial radius, there is a decline in the f_{EWcorot} . Thus, a key factor that determines how much of the CGM is co-rotating is its location within the halo and not its column density.

3.3 f_{EWcorot} and galaxy orientation

Our current picture of the CGM is one in which cool gas enters the galaxy halo preferentially along the galaxy’s major axis and likely accretes onto the galaxy while co-rotating with the disk (Stewart et al. 2011a,b, 2013; Nelson et al. 2016; Stewart et al. 2017; Suresh et al. 2019; Péroux et al. 2020). On the other hand, stellar winds and galaxy feedback will be ejected biconically along the minor axis of the galaxy with higher velocities than the disk (Bouché et al. 2012; Schroetter et al. 2016; Lan & Mo 2018; Schroetter et al. 2019; Reichardt Chu et al. 2022). Some observations have also shown that the spatial distribution of CGM around galaxies appears to be bimodal (Bordoloi et al. 2011; Bouché et al. 2012; Kacprzak et al. 2012b; Kacprzak et al. 2015; Lan et al. 2014; Dutta et al. 2017; Zabl et al. 2019). In order to further examine this picture and the relationships between gas flows with respect to their host galaxies, we explore how the co-rotation fraction relates to galaxy orientation and its behaviour as a function of column density and distance away from the galaxies.

Fig. 6 presents f_{EWcorot} as a function of D/R_{vir} and the azimuthal angle, Φ . Panels (a) and (b) are similar; however, while panel (a) shows the full sample, panel (b) plots only H I absorption systems within R_{vir} to focus on gas within the “halos” of these galaxies. The host galaxies are located at $D/R_{\text{vir}} = 0$ with their projected major axis aligned with $\Phi = 0$ deg. Each point represents H I absorption in a background quasar sightline and their sizes represent the absorption column densities to emphasise where the higher and lower column densities tend to reside. The anti-correlation between the H I column density and D/R_{vir} is clearly visible (also see Fig. 1). The points are also colour-coded based on the measured f_{EWcorot} in each system. The dark pink points in Fig. 6 have the highest consistency with co-rotation kinematics, while dark green is least consistent with the host galaxy rotation velocity.

From the figure, it is clear that the majority (56%) of our absorption systems reside within R_{vir} . On average, the absorption systems beyond R_{vir} tend to have a much lower f_{EWcorot} than within R_{vir} , with average f_{EWcorot} values of 0.39 and 0.58 outside and within R_{vir} , respectively. This is consistent with the idea that gas flows may be more organised nearer to galaxies and even that outflows mostly tend not to escape the halos of galaxies (Oppenheimer & Davé 2008; Tumlinson et al. 2011, 2013; Stocke et al. 2013). Within R_{vir} , absorption systems are consistent with higher f_{EWcorot} and tend to be found within 20 degree of galaxy major and minor axes and cover a large range of H I column densities. Furthermore, these high corotation fractions extend out to R_{vir} along both the major and minor axes. In the remaining part of this subsection, we further explore how f_{EWcorot} behaves with azimuthal and inclination angles as a function of column density and D/R_{vir} .

We next examine how f_{EWcorot} and azimuthal angle behaves with column density cuts. We apply the same bifurcation in column density of $\log(N(\text{H I})/\text{cm}^{-2}) = 14.5$ and $\log(N(\text{H I})/\text{cm}^{-2}) = 16.2$. Fig. 7 shows the f_{EWcorot} as a function of azimuthal angle with column densities bifurcated at $\log(N(\text{H I})/\text{cm}^{-2}) = 14.5$. The dark purple circles and light purple diamonds present the averaged f_{EWcorot} in bins of azimuthal angles (horizontal bars) for absorbers with $\log(N(\text{H I})/\text{cm}^{-2}) > 14.5$ and $\log(N(\text{H I})/\text{cm}^{-2}) \leq 14.5$, respectively, with 1σ bootstrap errors (vertical bars). Here the fainter data points in the background present individual systems where

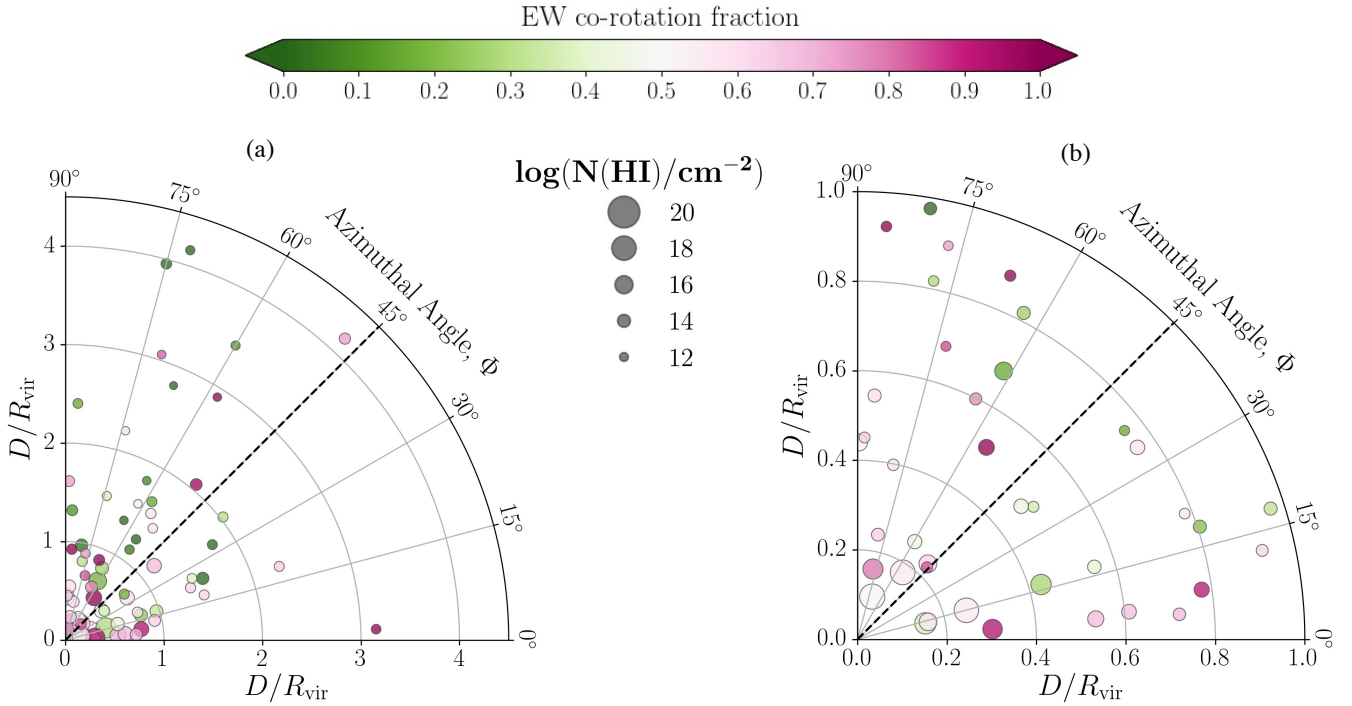


Figure 6. Virial radius normalised impact parameters (D/R_{vir}) vs. azimuthal angles (Φ). The host galaxies are located at $D/R_{\text{vir}} = 0$ with their major axis aligned with $\Phi = 0$ deg. Each coloured point represents H I absorption in a background quasar sightline. The absorption systems are colour coded by the equivalent width co-rotation fraction (f_{EWcorot}) where the darker pink and darker green represent high and low co-rotation fractions, respectively. The point sizes represent the column density of the systems where bigger circles show higher column density and smaller circles show the lower column density absorbers. (a) Distribution of quasar sightlines over the Φ and D/R_{vir} ranges. We find many systems with high co-rotation fraction ≥ 0.5 along both the major and minor axes of galaxies. (b) A zoomed-in version of the panel (a). Here we examine systems only within one virial radius of galaxies. We find more systems having kinematics consistent with co-rotation closer to the galaxies’ minor axis as well as the major axis.

the smaller purple circles show the systems with higher column densities ($\log(N(\text{HI})/\text{cm}^{-2}) > 14.5$) and the smaller light purple diamonds present absorbers with lower column densities ($\log(N(\text{HI})/\text{cm}^{-2}) \leq 14.5$). The high column density systems only have three bins due to the number of systems and sampling of the azimuthal angles. In general, we find that f_{EWcorot} is higher for high column density systems and lower for low column density systems, except within $\Phi = 20 - 30$ deg of the galaxy major axis where low column density systems have a higher f_{EWcorot} . Similarly, we find that the co-rotation fraction (f_{EWcorot}) for the $\log(N(\text{HI})/\text{cm}^{-2}) = 16.2$ cut has a higher average value for the high column density systems ($f_{\text{EWcorot}} \sim 0.62$) than for the low column density systems ($f_{\text{EWcorot}} \sim 0.46$). This trend remains flat across all azimuthal angles for the 16.2 column density cut (not shown here). We will discuss the implications of these results in the next section.

Given that we found f_{EWcorot} is more dependant on D/R_{vir} than D (see Fig. 5), we explore how f_{EWcorot} and azimuthal angle varies with D/R_{vir} . In Fig. 8 we present the f_{EWcorot} as a function of Φ where the sample is bifurcated at $D/R_{\text{vir}} = 1$. The orange circles and blue diamonds present the averaged f_{EWcorot} in bins of azimuthal angles (horizontal bars) for absorbers detected at $D/R_{\text{vir}} \leq 1$ and $D/R_{\text{vir}} > 1$, respectively, with 1σ bootstrap errors (vertical bars). The smaller data points in the background show individual systems where the blue diamonds are absorption detected inside the virial radius and the orange circles are the absorption detected outside the virial. The data show that along the projected galaxy major axis ($\Phi < 30$ deg), f_{EWcorot} has the same value inside

and outside the virial radius with just over half of the gas consistent with co-rotation. This may be expected if gas accretes along filaments, which are co-rotating/accreting from large-scale structure in the IGM down to the galaxy. As the azimuthal angle increases, f_{EWcorot} diverges. We find a high co-rotation fraction for H I gas in the R_{vir} CGM (orange) that slightly increases to a peak of 0.6 along the projected galaxy minor axis ($\Phi > 75$ deg). In contrast, H I detected at $D/R_{\text{vir}} > 1$ has a decreasing f_{EWcorot} with increasing Φ , where the value drops to 0.27 along the projected minor axis. This difference in f_{EWcorot} along the minor axis within and outside the virial radius is a factor of ~ 2 .

Thus, we find overall that only minor axis absorption ($\Phi \geq 60$ deg) yields significant variations of f_{EWcorot} with D/R_{vir} , whereas the major axis H I gas appears to have a flat distribution of f_{EWcorot} at all radii. If outflows are the dominant source of CGM gas along the minor axis, then outflowing gas co-rotates within the virial radius and either loses angular momentum with increasing height or fails to get to distances beyond the virial radius.

As our galaxies have a range of inclination angles, we investigate how f_{EWcorot} varies with galaxy inclination. In Fig. 9 we present f_{EWcorot} as a function of galaxy inclination angle, i , where the sample is bifurcated at $D/R_{\text{vir}} = 1$. We have verified that our sample’s distribution of inclination angles is consistent with a random distribution of galaxy inclination angles, and because of this, we have fewer galaxies at low inclination angles. The sample is split into three bins based on the inclination angle of the host galaxies: $i \leq 30$ deg, $30 < i \leq 60$ deg, and $i > 60$ deg. The orange circles show the averaged f_{EWcorot} in each inclination angle bin for

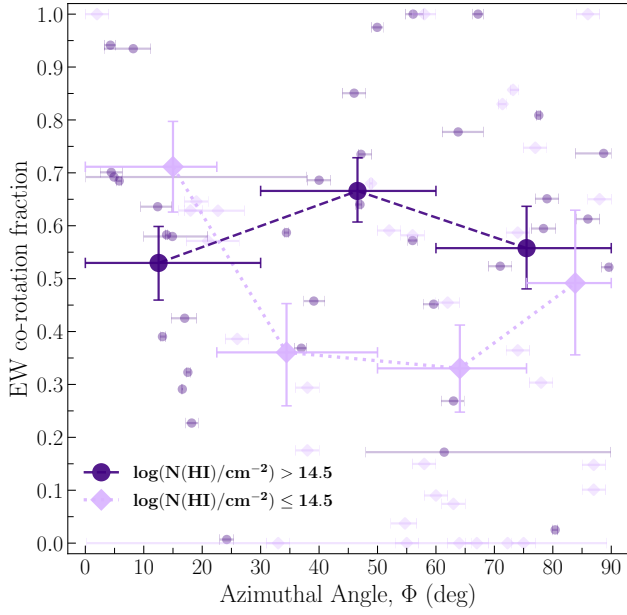


Figure 7. Equivalent width co-rotation fraction (f_{EWcorot}) as a function of azimuthal angle (Φ) for high (dark purple circles) and low (light purple diamonds) column density systems bifurcated at $\log(N(\text{H I})/\text{cm}^{-2}) = 14.5$. Smaller data points in the background present the individual absorption systems corresponding to each column density cut with the error bars representing the azimuthal angle errors. Absorption systems with $\log(N(\text{H I})/\text{cm}^{-2}) > 14.5$ in intermediate and high azimuthal angles bins have higher f_{EWcorot} , while in lower azimuthal angles, the f_{EWcorot} is larger for absorption systems with $\log(N(\text{H I})/\text{cm}^{-2}) \leq 14.5$. The f_{EWcorot} is consistent with a flat distribution across all azimuthal angles for the $\log(N(\text{H I})/\text{cm}^{-2}) = 16.2$ column density cut that is not shown here.

systems detected within the R_{vir} of the host galaxies (smaller pale orange data points in the background), while the blue diamonds present the averaged f_{EWcorot} in inclination angle bins for systems detected beyond the virial radius (smaller pale blue diamonds in the background). The vertical bars present the 1σ bootstrap errors. We find that the f_{EWcorot} of H I absorption within R_{vir} remains almost constant across all inclination angles within uncertainties. However, there is a possible trend that beyond R_{vir} , f_{EWcorot} drops at high inclination angles when compared to low and intermediate inclination angles. In highly inclined galaxies, f_{EWcorot} within the virial radius is a factor of ~ 2 higher when compared to H I gas beyond the virial radius. This result could be due to outflows not being able to travel beyond the virial radius and is consistent with what we found in Fig. 8 for the azimuthal angle trends.

3.4 f_{EWcorot} and halo mass

Some simulations predict that cold-mode accretion halts for halo masses of $\log(M_{\text{h}}/M_{\odot}) > 12$ (Dekel & Birnboim 2006; Kereš et al. 2009; Stewart et al. 2011a), which could present as lower H I co-rotation fractions for higher mass galaxies. Therefore, it is important to test how f_{EWcorot} varies with the halo mass. Our sample spans over two decades of halo mass from $10.5 < \log(M_{\text{h}}/M_{\odot}) < 12.7$, which allows us to test the simulation prediction. In Fig. 10 (a) and (b) we show the f_{EWcorot} as a function of stellar and halo mass, respectively. The grey data points in the background represent individual galaxies and the grey bars represent the stellar and halo

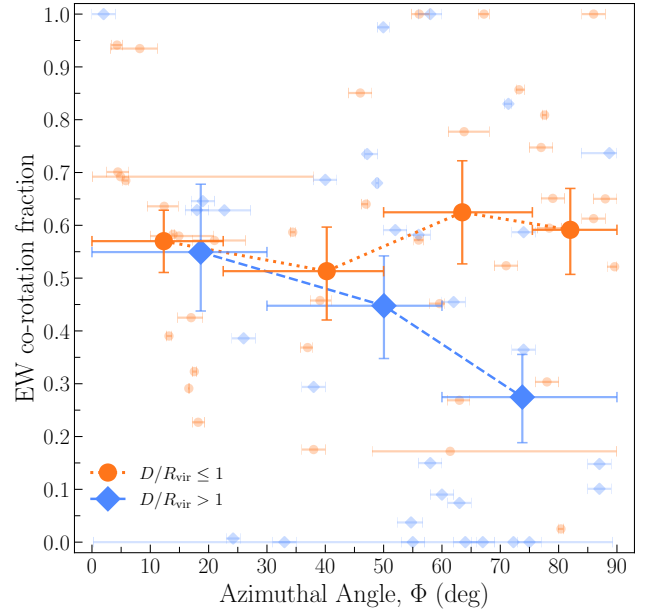


Figure 8. Equivalent width co-rotation fraction (f_{EWcorot}) as a function of azimuthal angle (Φ) for $D/R_{\text{vir}} > 1$ (blue diamonds) and $D/R_{\text{vir}} \leq 1$ (orange circles). Light orange circles and blue diamonds in the background represent the individual absorbers detected inside and outside the virial radius of host galaxies, respectively. The error bars on coloured data points in the background represent the azimuthal angle errors. While the f_{EWcorot} of systems within R_{vir} increases slightly with increasing Φ , the f_{EWcorot} of H I absorbers with $D/R_{\text{vir}} > 1$ decreases with increasing the azimuthal angle.

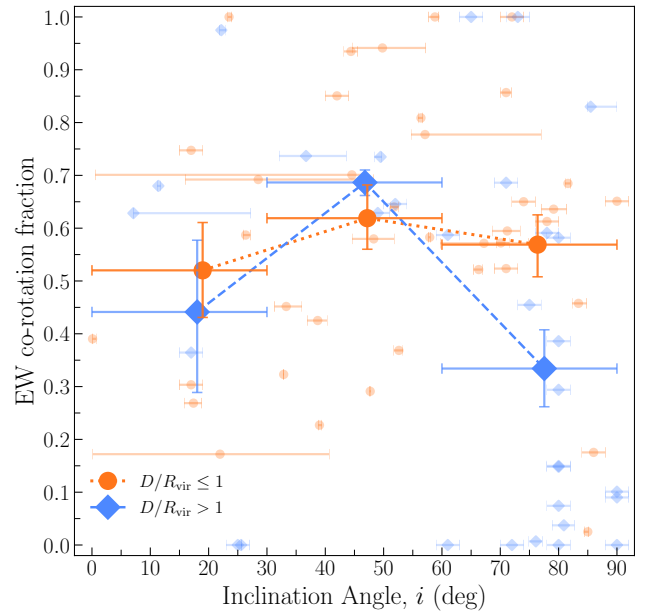


Figure 9. Equivalent width co-rotation fraction (f_{EWcorot}) as a function of inclination angle (i) for $D/R_{\text{vir}} > 1$ (blue diamonds) and $D/R_{\text{vir}} \leq 1$ (orange circles). The coloured data points in the background are individual galaxies and the error bars represent the inclination angle errors. The f_{EWcorot} of H I absorption within R_{vir} CGM remains almost constant with inclination angle. The f_{EWcorot} of H I absorbers at $D/R_{\text{vir}} > 1$ decreases for edge-on ($i \geq 60$ degrees) galaxies.

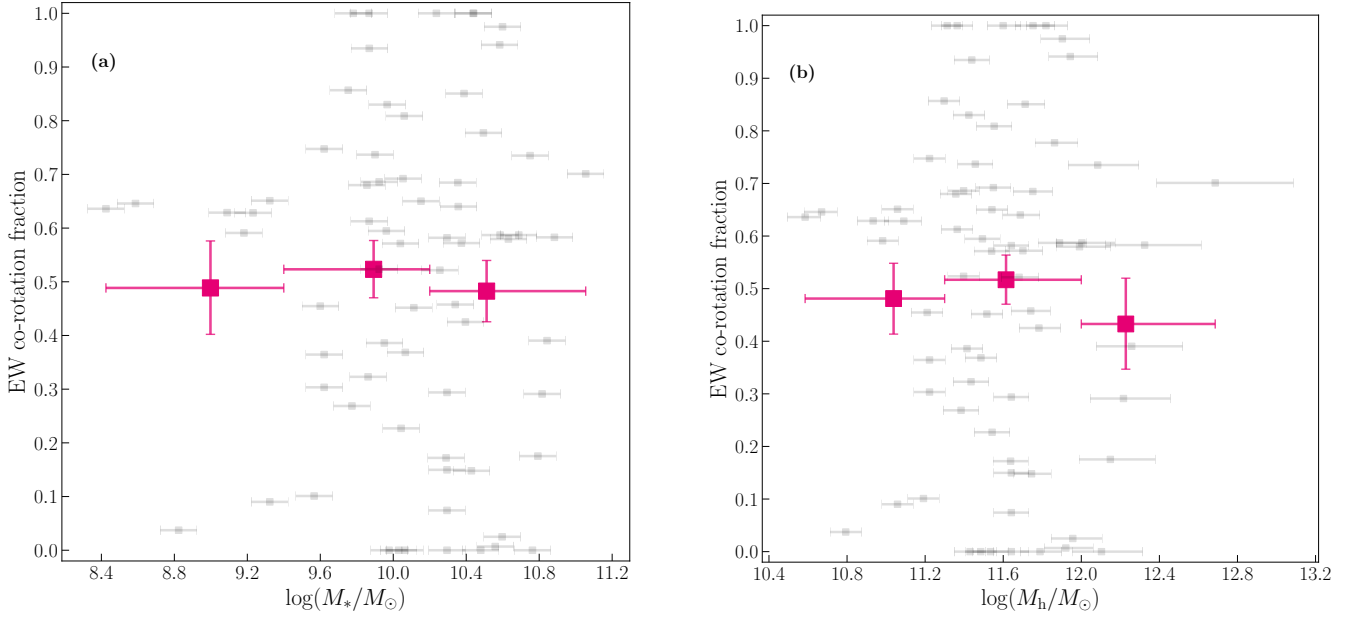


Figure 10. (a) H I absorption equivalent width co-rotation fraction (f_{EWcorot}) as a function of stellar mass. The grey data points are individual galaxies and the grey bars represent the mass errors. The galaxies are split into three stellar mass bins represented by horizontal bars. The pink squares show the averaged f_{EWcorot} in each bin and the 1σ errors (vertical bars) are measured using a bootstrap method. (b) Same as panel (a) except the f_{EWcorot} is a function of galaxies’ halo mass. The equivalent width co-rotation fraction is consistent with a flat distribution across the stellar and halo masses.

mass errors, respectively. The pink squares are the averaged f_{EWcorot} in mass bins (horizontal bars) with 1σ bootstrap errors (vertical bars). We do not find a significant dependence of f_{EWcorot} on galaxy stellar or halo mass. The data are consistent with being drawn from a flat distribution. Around $\sim 45\%$ of the H I gas is consistent with a co-rotation model at masses $M_h \geq 10^{12} M_\odot$, where simulations predict a truncation or halting of cold-mode co-rotating gas accretion. This could imply that the H I is consistent with being coupled to the kinematics of the galaxy at all masses and/or that accretion is present in galaxies of all masses for our sample. It is also possible that the kinematic connection at higher masses is due to the motions of the larger scale environment that those galaxies live in.

4 DISCUSSION

H I observations of galactic disks and halos provide new insights into gas flows in the local universe. Feedback, cosmic web filaments, surrounding H I cloud complexes, and minor mergers can all drive the presence and kinematics of gas found in the CGM. It is expected that the connection between the galaxy and CGM kinematics reflects the types of ongoing processes within this diverse gaseous ecosystem. Targeting 70 H I absorption systems assists us in directly probing cool metal-enriched CGM gas over 8 decades of H I column density that is sensitive to a vast range of CGM processes. Using a co-rotating halo assumption to quantify the amount of H I co-rotating gas, we have explored how the kinematics of the CGM relates to the host galaxy properties in an effort to address the origins of this gas.

4.1 Interpretation of co-rotation fraction and column density and distance

The H I column density is an important measure of the CGM as it provides insight into where the gas is located and where it originated from. [Rudie et al. \(2012\)](#) determined that $\log(N(\text{H I})/\text{cm}^{-2}) < 14.5$ most probably traces distant IGM gas while cosmological simulations have shown that $\log(N(\text{H I})/\text{cm}^{-2}) > 16$ is primarily found in the CGM gas flows within the halos of galaxies (e.g., [Fumagalli et al. 2011](#); [Suresh et al. 2019](#)). We found that there is a correlation between f_{EWcorot} and $N(\text{H I})$ in Fig. 3 where there is an increase in f_{EWcorot} by a factor of ~ 1.5 from the lowest column density systems to the highest column density systems. This correlation likely implies that there is some dependence on co-rotation and physical processes in a halo, such as outflows from the galaxy, accretion from the IGM, recycled accretion and diffuse components of the CGM. If CGM gas flows exhibit the bulk of the co-rotating gas, then our results are in line with the simulation predictions that higher column density systems are better tracers of gas flows. However, the H I column density is strongly correlated with the impact parameter and is a hidden additional parameter not accounted for in Fig. 3.

To examine dependencies with absorption location with respect to the host galaxy, we studied the f_{EWcorot} as a function of D and D/R_{vir} . We found no significant difference between the statistical behaviour of low and high column density systems over a large range of impact parameters (see Fig. 4). However, the scatter in these trends could be significant given the large range of galaxy masses in the sample. We removed the impact of the host galaxies’ mass by probing the co-rotation fraction as a function of the virial radius normalised impact parameter (see Fig. 5). We showed that the co-rotation fraction is almost constant within the CGM and drops by a factor of two outside of the virial radii of galaxies. This implies that the H I is most kinematically connected to galaxies within the halo, where most of the physical processes are expected to occur (e.g., outflows, tidal streams, recycling, accretion, etc.). Thus, both

column density and distance from the galaxy play critical roles in where gas is kinematically connected to their galaxies. Nonetheless, there is still 35% of H I that is consistent with co-rotation out to $3R_{\text{vir}}$. This gas could be probing filamentary accretion or larger-scale movements of the local environment.

Our results are consistent with the findings of previous works. French & Wakker (2020) reported a co-rotation fraction of $59 \pm 5\%$ for low column density Ly α absorbers. Although we use a new method, and our samples overlap at low column densities, the results do not show any significant differences. The authors also reported a decrease in the co-rotation fraction as a function of the impact parameter. However, what we additionally noted here is that both column density and D/R_{vir} are significant factors in the behaviour of f_{EWcorot} , with an important transition occurring at R_{vir} , where the co-rotation fraction changes from a roughly constant value to rapidly decreasing.

Our co-rotation fractions are also consistent with those found for Mg II absorption systems (Steidel et al. 2002; Kacprzak et al. 2010, 2011b; Ho et al. 2017; Martin et al. 2019), which is not so surprising since Mg II and H I likely trace similar structures and densities. The main difference between the findings for the two gas tracers is that Mg II absorption tends to have the majority of the absorption aligned with the rotation of the galaxy (Steidel et al. 2002; Kacprzak et al. 2010; Ho et al. 2017), while H I exhibits a wide range of co-rotation values (see scatter in Fig. 1). This could be due to the fact that Mg II directly traces higher column density H I that has some metal enrichment where, as we have shown, this higher column density H I has a higher co-rotation fraction. On the other hand, the H I absorption is more spatially widespread than Mg II, and traces a larger range of column densities, which could be tracing CGM/IGM or a diffuse component of the CGM, etc., along the same sightline, which has been shown to occur within cosmological simulations (Churchill et al. 2015; Peebles et al. 2019; Marra et al. 2021, 2022). The lower column density H I can also be traced by O VI, which has lower co-rotation values of $\sim 50\%$ (Kacprzak et al. 2019a). We will explore the co-rotation fraction of the metals for our sample in an upcoming paper. Overall, our observations are consistent with those from the literature, which provide a picture of the CGM where we find a stronger kinematic connection to the CGM with higher column densities close to the galaxies and weaker kinematic connection to the CGM with lower column densities further from the galaxies.

4.2 Interpretation of co-rotation fraction and galaxy orientation

Our kinematic analysis of H I absorption also supports a non-uniform and likely bi-modal picture of CGM around galaxies. By accounting for the distance away from galaxies, we found that the co-rotation fraction increases with increasing azimuthal angle within R_{vir} and decreases with increasing azimuthal angle beyond R_{vir} (Fig. 8). This is further supported by a similar trend for galaxy inclination angle, where the co-rotation fraction decreases the most at large inclination angles for gas outside R_{vir} (Fig. 9). There appears to be a geometric preference for co-rotating gas around galaxies, especially along the minor axis and within R_{vir} . Compared to previous results, French & Wakker (2020) also reported a sharp decrease in their measure of co-rotation fraction above $i > 70$ deg, which is consistent with our results for gas outside R_{vir} . They likely only saw a decrease since the majority of their sample is low column density H I gas that resides near-to-outside of the virial radius.

Tying together all of our results and motivations from previous

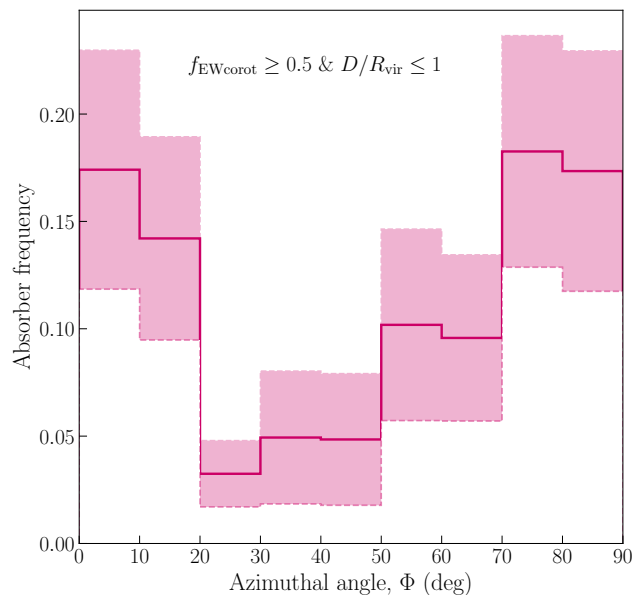


Figure 11. Azimuthal distribution of H I CGM absorption systems within R_{vir} with high co-rotation fraction ($f_{\text{EWcorot}} \geq 0.5$). The solid pink line represents the observed frequency in each Φ bin and the shaded region represents the 1σ error measured by bootstrapping the sample. The data suggest a bimodal distribution for CGM absorption with high co-rotation fractions where the histogram peaks along the major and minor axes.

works, we further examine the geometric distribution of co-rotating gas. We computed the frequency of absorption systems as a function of azimuthal angle in Fig. 11, focusing on systems dominated by co-rotating gas (e.g., the "bulk" of the gas where $f_{\text{EWcorot}} \geq 0.5$, which would be similar to other works) within the virial radius of galaxies. Following the methods of Kacprzak et al. (2012b) and Kacprzak et al. (2015), we model the measured azimuthal angles and their uncertainties for each of the galaxies as asymmetric univariate Gaussian PDFs (see Kato et al. 2002). We then compute the mean PDF of all galaxies as a function of Φ . The mean PDF represents the absorption frequency of co-rotating gas at a given Φ . The resulting PDF plotted in Fig. 11 may be bimodal, where the frequency of highly co-rotating gas within R_{vir} is elevated along the major axis and is highly elevated along the minor axis. This distribution mimics the Mg II and O VI covering fraction bi-modalities, which were assumed to be caused by accretion along the major axis and outflows along the minor axis (Kacprzak et al. 2012b; Kacprzak et al. 2015).

The most surprising aspect of our results with azimuthal angle is that we see significant co-rotation along the minor axis, where gas is often assumed to be outflowing from the galaxy. Fig. 8 further supports the inference that the minor axis co-rotation is dominated by outflows since we find that f_{EWcorot} diverges with increasing azimuthal angle inside and outside the virial radius. If outflows dominate along the minor axes of galaxies, then they appear to have a higher level of co-rotation within the virial radius, suggesting that outflows travel up to R_{vir} , but the drop in co-rotation beyond the virial radius suggests that most outflows do not escape. This is consistent with the relative galaxy-absorption velocities which tend to be below the escape velocity of galaxy halos (Stocke et al. 2013; Mathes et al. 2014).

Our co-rotating outflow signatures are in contrast to previous emission line maps of outflowing gas, which tend to show a rapid

decrease in the rotation velocities along the minor axis to within a few 10 – 20 kpc. Outflows from local starbursting galaxies suggest that signatures of co-rotation diminish beyond 1 kpc from M82 in CO (Leroy et al. 2015). However, rotating gas was found along the outflow axis in recent Enzo (FOGGIE) simulations (Lochhaas et al. 2023). Mapping the gas around a more normal star-forming galaxy in Mg II, [O II], and [O III] emission, Zabl et al. (2021) did not find any co-rotation signatures beyond 10 kpc. However, the ionisation mechanism for the Mg II and nebular emission is still unknown, so our CGM observations do not necessarily trace the same gas, and the starbursting galaxies have higher star formation rates than our sample, which could result in different outflow kinematic properties. In more comparable work, Martin et al. (2019) reported no correlation between the sign of the Doppler shift of Mg II absorption and the rotation of galaxies along the minor axis. This difference could be due to a difference in Mg II/H I gas tracers or most likely, how co-rotation fractions are defined and measured. Kacprzak et al. (2012a) reported low metallicity (~ -2 dex) multi-phase accretion along the minor axis. They found that the low ionisation ions, like Mg II and Si II, were consistent with co-rotation, while the higher ionisation features, like C III, C IV, and O VI, contained both co-rotating gas as well as a fraction of gas that is inconsistent with co-rotation. This again points to a picture where co-rotation likely depends on H I column density.

If gas accretion via filaments is instead driving the co-rotation seen along the minor axis, then we would expect high co-rotation fractions both inside and outside the virial radius since the accretion is originating from the IGM. However, Fig. 8 clearly shows this to not be the case. Accretion more likely explains the major axis kinematic and co-rotation fraction trends where we do not see any significant transition in kinematics as a function of R_{vir} , which is expected from simulations where co-rotation is seen beyond the virial radius (Danovich et al. 2015; Stewart et al. 2013, 2017).

From another perspective, the significant drop in co-rotation at larger distances along the minor axis, is interesting in itself. It is intriguing that there is a significant amount of gas that have kinematics opposite to the rotation of galaxies. One possibility is that this gas could arise from ancient debris from previous galaxies interactions, which can produce retrograde orbits or reversed kinematics. For example, N-body simulations of NGC 7252 and NGC 3921 are able to reproduce the reversal kinematics observed in their low H I column density tidal tails (Hibbard & Mihos 1995; Hibbard & van Gorkom 1996). Numerical studies of Milky-way also find counter-rotating material around the Galaxy as a result of interactions between disk galaxies. Modelling of interactions implies that merger or fly-by can produce material with retrograde orbits (Pawlowski et al. 2011). This retrograde motion of satellites seems to be quite common in a sample of $z < 0.04$ SDSS galaxies, which was shown that 40% of the galaxies have retrograde motions, which is the same fraction seen in cosmological simulations (Azzaro et al. 2006). Therefore, it is plausible to find low column density gas in retrograde motion at large distances, but it is strange that we see this occurring around the minor axes of our more isolated sample of galaxies. This may only occur if the alignment of the large scale structure is in the direction of the minor axes of these galaxies (Bailin et al. 2008). A larger statistical sample would help to explore this discovery.

Another interesting finding shown in Fig. 7 is that while there is the expected lower f_{EWcorot} for lower column density systems, it is not true along the major axes of galaxies. f_{EWcorot} jumps by nearly a factor of two for lower column density systems, while high column density systems have a lower f_{EWcorot} . This could possibly be due to the fragmentation of clouds as they approach the disk or within

an accretion stream. One would expect this to occur along the minor axis as well since simulations have shown clouds can fragment as they move through outflows (McCourt et al. 2018; Sparre et al. 2018; Nelson et al. 2020). So it is unclear why we see a transition along the major axis and not the minor axis.

4.3 Interpretation of co-rotation fraction and halo mass

Churchill et al. (2013b) studied the relation between Mg II equivalent width and host galaxies' virial mass and found no anti-correlation. Despite the prediction of simulations (van de Voort et al. 2011; Stewart et al. 2011a), the strength of low-ionisation CGM absorption is not dependent on halo mass and there is no sudden truncation of cold-mode accretion at a mass of $\log(M_{\text{h}}/M_{\odot}) = 12$. It is interesting that our results for f_{EWcorot} as a function of $\log(M_{\text{h}}/M_{\odot})$ are roughly constant. If we assume that the co-rotating gas is associated with cold-mode accretion, then gas accretion is not dependent on halo mass and cold-mode accretion is still occurring in the most massive galaxy halos.

It is plausible that the existence of cool gas for high mass galaxies could be arising from their environment, i.e., arising from the galaxies surrounding them. However, here we find the majority of the gas within R_{vir} is kinematically consistent with galaxy co-rotation. Given that the vast majority of Mg II absorption is found within R_{vir} , and that we find most of the gas with R_{vir} is kinematically coupled to the galaxy, then it is less likely that the CGM detected in high mass galaxies arises from larger-scale environments like groups and clusters since they would have larger velocity offsets and could be inconsistent with a co-rotation model. Environmental effects may be more significant for gas outside R_{vir} , where there is 35% out at $3 R_{\text{vir}}$, but this does not represent the bulk of the total absorption seen in the CGM.

5 CONCLUSIONS

We developed a new method for quantifying the amount of absorption that is consistent with a co-rotation model to examine the kinematic processes within the CGM. In this work, we analysed 70 quasar sightlines with H I absorption detected in their *HST/COS* spectra around 62, $z < 0.6$, isolated galaxies. Our sample spans a wide range of column densities, $12 < \log(N(\text{H I})/\text{cm}^{-2}) < 20$, likely associated with both the IGM and CGM. We either measured the rotation curve of galaxies using their Keck/ESI spectra or collected them from literature and connected the spin of galaxies to their H I absorption kinematics. We measured the fraction of H I gas that is aligned with galaxy rotation and examined the H I co-rotation fraction (f_{EWcorot}) as a function of absorption properties such as column density, projected distance from the galaxy (D and D/R_{vir}), and its location with respect to galaxies' major axis (Φ), and galaxy properties like inclination angle (i) and mass ($\log(M_{\text{h}}/M_{\odot})$). Our results include the following:

- (i) The co-rotation fraction of H I absorption is correlated with its column density. f_{EWcorot} ranges from ~ 0.4 for low column density systems ($\langle \log(N(\text{H I})/\text{cm}^{-2}) \rangle \sim 14$) to ~ 0.6 for high column density systems ($\langle \log(N(\text{H I})/\text{cm}^{-2}) \rangle \sim 18$). This implies that as the column density increases, the CGM is more coupled to the kinematics of the galaxy and may be more associated with accreting or outflowing gas, however it is important to account for D/R_{vir} in this relation.

(ii) There is no strong correlation between f_{EWcorot} and impact parameter, even when we examine the relation for low and high column density systems. Instead, it is imperative to consider galaxy halo mass and normalise the impact parameter by a galaxy's virial radius when connecting the CGM to its galaxy. This is because there is a relationship between the f_{EWcorot} and D/R_{vir} where there is a flat distribution with $f_{\text{EWcorot}} \sim 0.6$ within the virial radius. Beyond the virial radius, where the absorption is dominated by lower column density systems, f_{EWcorot} decreases within increasing D/R_{vir} and $f_{\text{EWcorot}} = 0.35$ at the largest distances. These two trends are present when the sample is split by both low ($\log(N(\text{H I})/\text{cm}^{-2}) = 14.5$) and high ($\log(N(\text{H I})/\text{cm}^{-2}) = 16.2$) column densities to separate out the IGM/CGM contributions and the diffuse gas versus gas flow contributions, respectively.

(iii) Along the major axis $f_{\text{EWcorot}} \sim 0.55$ regardless of distance from the galaxy but this value diverges with increasing azimuthal angle inside and outside the virial radius. Within the virial radius, f_{EWcorot} increases to a peak of 0.6 at $\Phi = 90$ deg, while outside of the virial radius, f_{EWcorot} decreases to a minimum of 0.27 at $\Phi = 90$ deg. If this divergence is caused by outflows, then this could imply that the minor axis gas within R_{vir} is bound and co-rotating with the host galaxy while the gas beyond R_{vir} has less of a co-rotation signature and could be IGM gas.

(iv) f_{EWcorot} shows a similar behaviour with galaxy inclination for face-on galaxies regardless of distance from the galaxy, but the value diverges for edge-on galaxies to $f_{\text{EWcorot}} = 0.6$ for H I within the virial radius and $f_{\text{EWcorot}} = 0.3$ outside the virial radius. This may indicate that the cross-section of outflows decreases outside of the virial radius.

(v) If we examine only H I gas that is dominated by co-rotation ($f_{\text{EWcorot}} > 0.5$) and is within the virial radius of galaxies, we find a non-uniform and likely bimodal azimuthal distribution where the gas is preferentially located along the galaxy projected major and minor axes. This result mimics previous covering fraction results with azimuthal angle for both Mg II and O VI absorption. Together these findings suggest that gas flows such as accretion and outflows, respectively, are most likely to be found and kinematically connected to host galaxies within R_{vir} .

(vi) There is a significant fraction of co-rotating gas along the minor axis. If this is where outflows are expected, then the outflowing gas maintains rotation out to large fractions of the virial radius. This result is in contrast with previous emission mapping of outflows in Mg II and nebular emission for more highly star-forming galaxies, where the gas only co-rotates out to at most 10 – 20 kpc. This difference suggests that emission and absorption trace different gas and/or that increased star formation rates reduce the amount of co-rotation in outflows.

(vii) The H I co-rotation fraction is flat with galaxy stellar and halo mass. This is inconsistent with simulations that predict suppression of H I gas and accretion in massive halos.

In this work, we examined how the column density and kinematics of H I gas in the CGM relate to galaxy kinematics. We suggest that the different H I column densities probed by Mg II and O VI resulted in the different kinematics signatures detected in previous studies. As H I tracks both the low and high ionisation CGM, our results likely explain some of the disparity in previous studies. Thus, H I is likely the best way to study the full range of dynamical processes in the CGM. In the future, we will explore how the metals behave for these systems, especially how the co-rotation fraction changes with different ions. We will also examine how different co-rotation and outflow models affect the co-rotation fraction in

an effort to understand how much gas accretion and gas outflow is occurring within halos.

ACKNOWLEDGEMENTS

We acknowledge the efforts by the Editor who helped improve the quality of the paper. We thank David French for kindly providing the error values used in their paper. H.N, G.G.K, and N.M.N. acknowledge the support of the Australian Research Council Centre of Excellence for All Sky Astrophysics in 3 Dimensions (ASTRO 3D), through project number CE170100013. Some of the data presented herein were obtained at the W. M. Keck Observatory, which is operated as a scientific partnership among the California Institute of Technology, the University of California and the National Aeronautics and Space Administration. The Observatory was made possible by the generous financial support of the W. M. Keck Foundation. Observations were supported by Swinburne Keck programs with 2010A_W007E, 2010B_W032E, 2014A_W178E, 2014B_W018E, 2015_W187E, and 2016A_W056E. The authors wish to recognise and acknowledge the very significant cultural role and reverence that the summit of Maunakea has always had within the indigenous Hawaiian community. We are most fortunate to have the opportunity to conduct observations from this mountain.

DATA AVAILABILITY

The data underlying this paper will be shared on reasonable request to the corresponding author.

REFERENCES

- Azzaro M., Zentner A. R., Prada F., Klypin A. A., 2006, *ApJ*, **645**, 228
 Bailin J., Power C., Norberg P., Zaritsky D., Gibson B. K., 2008, *MNRAS*, **390**, 1133
 Barcons X., Lanzetta K. M., Webb J. K., 1995, *Nature*, **376**, 321
 Bell E. F., McIntosh D. H., Katz N., Weinberg M. D., 2003, *ApJS*, **149**, 289
 Blanton M. R., Roweis S., 2007, *AJ*, **133**, 734
 Bordoloi R., et al., 2011, *ApJ*, **743**, 10
 Bordoloi R., Prochaska J. X., Tumlinson J., Werk J. K., Tripp T. M., Burchett J. N., 2018, *ApJ*, **864**, 132
 Borthakur S., et al., 2015, *ApJ*, **813**, 46
 Bouché N., Hohensee W., Vargas R., Kacprzak G. G., Martin C. L., Cooke J., Churchill C. W., 2012, *MNRAS*, **426**, 801
 Bouché N., Murphy M. T., Kacprzak G. G., Péroux C., Contini T., Martin C. L., Dessauges-Zavadsky M., 2013, *Science*, **341**, 50
 Bouché N., et al., 2016, *ApJ*, **820**, 121
 Bouma S. J. D., Richter P., Wendt M., 2021, *A&A*, **647**, A166
 Bryan G. L., Norman M. L., 1998, *ApJ*, **495**, 80
 Burchett J. N., Tripp T. M., Werk J. K., Howk J. C., Prochaska J. X., Ford A. B., Davé R., 2013, *ApJ*, **779**, L17
 Carswell R. F., Webb J. K., 2014, VPFIT: Voigt profile fitting program, Astrophysics Source Code Library, record ascl:1408.015 (ascl:1408.015)
 Chambers K. C., et al., 2016, arXiv e-prints, p. arXiv:1612.05560
 Chen H.-W., Helsby J. E., Gauthier J.-R., Sheiman S. A., Thompson I. B., Tinker J. L., 2010, *ApJ*, **714**, 1521
 Churchill C. W., 1997, PhD thesis, Univ. California, Santa Cruz
 Churchill C. W., Vogt S. S., 2001, *AJ*, **122**, 679
 Churchill C. W., Nielsen N. M., Kacprzak G. G., Trujillo-Gomez S., 2013a, *ApJ*, **763**, L42
 Churchill C. W., Trujillo-Gomez S., Nielsen N. M., Kacprzak G. G., 2013b, *ApJ*, **779**, 87
 Churchill C. W., Vander Vliet J. R., Trujillo-Gomez S., Kacprzak G. G., Klypin A., 2015, *ApJ*, **802**, 10

- Côté S., Wyse R. F. G., Carignan C., Freeman K. C., Broadhurst T., 2005, *ApJ*, **618**, 178
- Danforth C. W., Stocke J. T., Shull J. M., 2010, *ApJ*, **710**, 613
- Danovich M., Dekel A., Hahn O., Ceverino D., Primack J., 2015, *MNRAS*, **449**, 2087
- Dekel A., Birnboim Y., 2006, *MNRAS*, **368**, 2
- Dekel A., et al., 2009, *Nature*, **457**, 451
- Dey A., et al., 2019, *AJ*, **157**, 168
- Diamond-Stanic A. M., Coil A. L., Moustakas J., Tremonti C. A., Sell P. H., Mendez A. J., Hickox R. C., Rudnick G. H., 2016, *ApJ*, **824**, 24
- Dutta R., Srianand R., Gupta N., Momjian E., Noterdaeme P., Petitjean P., Rahmani H., 2017, *MNRAS*, **465**, 588
- Faucher-Giguère C.-A., Kereš D., 2011, *MNRAS*, **412**, L118
- Faucher-Giguère C.-A., Hopkins P. F., Kereš D., Muratov A. L., Murray N., 2015, *MNRAS*, **449**, 987
- Fernández-Figueroa A., Kacprzak G. G., Nielsen N. M., Barone T. M., Nateghi H., Sameer Fisher D. B., Chu B. R., 2024, *MNRAS*, **531**, 3658
- French D. M., Wakker B. P., 2020, *ApJ*, **897**, 151
- Fumagalli M., Prochaska J. X., Kasen D., Dekel A., Ceverino D., Primack J. R., 2011, *MNRAS*, **418**, 1796
- Girelli G., Pozzetti L., Bolzonella M., Giocoli C., Marulli F., Baldi M., 2020, *A&A*, **634**, A135
- Hafen Z., et al., 2017, *MNRAS*, **469**, 2292
- Hibbard J. E., Mihos J. C., 1995, *AJ*, **110**, 140
- Hibbard J. E., van Gorkom J. H., 1996, *AJ*, **111**, 655
- Ho S. H., Martin C. L., Kacprzak G. G., Churchill C. W., 2017, *ApJ*, **835**, 267
- Hobbs A., Read J., Nicola A., 2015, *MNRAS*, **452**, 3593
- Jorgenson R. A., Wolfe A. M., 2014, *ApJ*, **785**, 16
- Kacprzak G. G., Churchill C. W., Ceverino D., Steidel C. C., Klypin A., Murphy M. T., 2010, *ApJ*, **711**, 533
- Kacprzak G. G., Churchill C. W., Evans J. L., Murphy M. T., Steidel C. C., 2011a, *Monthly Notices of the Royal Astronomical Society*, **416**, 3118
- Kacprzak G. G., Churchill C. W., Barton E. J., Cooke J., 2011b, *ApJ*, **733**, 105
- Kacprzak G. G., Churchill C. W., Steidel C. C., Spitler L. R., Holtzman J. A., 2012a, *MNRAS*, **427**, 3029
- Kacprzak G. G., Churchill C. W., Nielsen N. M., 2012b, *The Astrophysical Journal*, **760**, L7
- Kacprzak G. G., Muzahid S., Churchill C. W., Nielsen N. M., Charlton J. C., 2015, *ApJ*, **815**, 22
- Kacprzak G. G., et al., 2019a, *ApJ*, **870**, 137
- Kacprzak G. G., Pointon S. K., Nielsen N. M., Churchill C. W., Muzahid S., Charlton J. C., 2019b, *ApJ*, **886**, 91
- Kacprzak G. G., Nielsen N. M., Nateghi H., Churchill C. W., Pointon S. K., Nanayakkara T., Muzahid S., Charlton J. C., 2021, *MNRAS*, **500**, 2289
- Kato T., Omachi S., Aso H., 2002, in Caelli T., Amin A., Duin R. P. W., de Ridder D., Kamel M., eds, *Structural, Syntactic, and Statistical Pattern Recognition*. Springer Berlin Heidelberg, Berlin, Heidelberg, pp 405–413
- Kereš D., Katz N., Weinberg D. H., Davé R., 2005, *MNRAS*, **363**, 2
- Kereš D., Katz N., Fardal M., Davé R., Weinberg D. H., 2009, *MNRAS*, **395**, 160
- Lan T.-W., Mo H., 2018, *ApJ*, **866**, 36
- Lan T.-W., Ménard B., Zhu G., 2014, *ApJ*, **795**, 31
- Langan I., et al., 2023, arXiv e-prints, p. arXiv:2301.10779
- Law D. R., Steidel C. C., Erb D. K., Larkin J. E., Pettini M., Shapley A. E., Wright S. A., 2009, *ApJ*, **697**, 2057
- Lehner N., et al., 2013, *ApJ*, **770**, 138
- Lehner N., Wotta C. B., Howk J. C., O’Meara J. M., Oppenheimer B. D., Cooksey K. L., 2018, *ApJ*, **866**, 33
- Leroy A. K., et al., 2015, *ApJ*, **814**, 83
- Lochhaas C., et al., 2023, *ApJ*, **948**, 43
- Lopez S., et al., 2020, *MNRAS*, **491**, 4442
- Marra R., et al., 2021, *MNRAS*, **508**, 4938
- Marra R., Churchill C. W., Kacprzak G. G., Nielsen N. M., Trujillo-Gomez S., Lewis E., 2022, arXiv e-prints, p. arXiv:2202.12228
- Martin C. L., Ho S. H., Kacprzak G. G., Churchill C. W., 2019, *ApJ*, **878**, 84
- Marzke R. O., Huchra J. P., Geller M. J., 1994, *ApJ*, **428**, 43
- Massa D., et al. 2013, COS Data Handbook v. 2.0
- Mathes N. L., Churchill C. W., Kacprzak G. G., Nielsen N. M., Trujillo-Gomez S., Charlton J., Muzahid S., 2014, *ApJ*, **792**, 128
- McCourt M., Oh S. P., O’Leary R., Madigan A.-M., 2018, *MNRAS*, **473**, 5407
- Nateghi H., Kacprzak G. G., Nielsen N. M., Muzahid S., Churchill C. W., Pointon S. K., Charlton J. C., 2021, *MNRAS*, **500**, 3987
- Nelson D., Genel S., Pillepich A., Vogelsberger M., Springel V., Hernquist L., 2016, *MNRAS*, **460**, 2881
- Nelson D., et al., 2020, *MNRAS*, **498**, 2391
- Ng M., Nielsen N. M., Kacprzak G. G., Pointon S. K., Muzahid S., Churchill C. W., Charlton J. C., 2019, *ApJ*, **886**, 66
- Nielsen N. M., Churchill C. W., Kacprzak G. G., Murphy M. T., 2013, *ApJ*, **776**, 114
- Nielsen N. M., Kacprzak G. G., Muzahid S., Churchill C. W., Murphy M. T., Charlton J. C., 2017, *The Astrophysical Journal*, **834**, 148
- Nielsen N. M., Kacprzak G. G., Pointon S. K., Churchill C. W., Murphy M. T., 2018, *ApJ*, **869**, 153
- Nielsen N. M., Kacprzak G. G., Sameer Murphy M. T., Nateghi H., Charlton J. C., Churchill C. W., 2022, *MNRAS*, **514**, 6074
- Oppenheimer B. D., Davé R., 2008, *MNRAS*, **387**, 577
- Oppenheimer B. D., et al., 2016, *Monthly Notices of the Royal Astronomical Society*, **460**, 2157
- Pawlowski M. S., Kroupa P., de Boer K. S., 2011, *A&A*, **532**, A118
- Peeples M. S., et al., 2019, *ApJ*, **873**, 129
- Péroux C., Nelson D., van de Voort F., Pillepich A., Marinacci F., Vogelsberger M., Hernquist L., 2020, *MNRAS*, **499**, 2462
- Pointon S. K., Nielsen N. M., Kacprzak G. G., Muzahid S., Churchill C. W., Charlton J. C., 2017, *The Astrophysical Journal*, **844**, 23
- Pointon S. K., Kacprzak G. G., Nielsen N. M., Muzahid S., Murphy M. T., Churchill C. W., Charlton J. C., 2019, *ApJ*, **883**, 78
- Rahmani H., et al., 2018, *MNRAS*, **474**, 254
- Reichardt Chu B., et al., 2022, *MNRAS*, **511**, 5782
- Rudie G. C., et al., 2012, *ApJ*, **750**, 67
- Sameer et al., 2021, *MNRAS*, **501**, 2112
- Sameer et al., 2024, *MNRAS*, **530**, 3827
- Schroetter I., et al., 2016, *The Astrophysical Journal*, **833**, 39
- Schroetter I., et al., 2019, *MNRAS*, **490**, 4368
- Sheinis A. I., Bolte M., Epps H. W., Kibrick R. I., Miller J. S., Radovan M. V., Bigelow B. C., Sutin B. M., 2002, *PASP*, **114**, 851
- Simard L., et al., 2002, *The Astrophysical Journal Supplement Series*, **142**, 1
- Sparre M., Pfrommer C., Vogelsberger M., 2018, *Monthly Notices of the Royal Astronomical Society*, **482**, 5401
- Steidel C. C., Dickinson M., Persson S. E., 1994, *ApJ*, **437**, L75
- Steidel C. C., Kollmeier J. A., Shapley A. E., Churchill C. W., Dickinson M., Pettini M., 2002, *ApJ*, **570**, 526
- Stewart K. R., Kaufmann T., Bullock J. S., Barton E. J., Maller A. H., Diemand J., Wadsley J., 2011a, *ApJ*, **735**, L1
- Stewart K. R., Kaufmann T., Bullock J. S., Barton E. J., Maller A. H., Diemand J., Wadsley J., 2011b, *ApJ*, **738**, 39
- Stewart K. R., Brooks A. M., Bullock J. S., Maller A. H., Diemand J., Wadsley J., Moustakas L. A., 2013, *ApJ*, **769**, 74
- Stewart K. R., et al., 2017, *ApJ*, **843**, 47
- Stocke J. T., Keeney B. A., Danforth C. W., Shull J. M., Froning C. S., Green J. C., Penton S. V., Savage B. D., 2013, *ApJ*, **763**, 148
- Suresh J., Nelson D., Genel S., Rubin K. H. R., Hernquist L., 2019, *MNRAS*, **483**, 4040
- Tripp T. M., Sembach K. R., Bowen D. V., Savage B. D., Jenkins E. B., Lehner N., Richter P., 2008, *ApJS*, **177**, 39
- Tumlinson J., et al., 2011, *Science*, **334**, 948
- Tumlinson J., et al., 2013, *ApJ*, **777**, 99
- Vogt N. P., Forbes D. A., Phillips A. C., Gronwall C., Faber S. M., Illingworth G. D., Koo D. C., 1996, *ApJ*, **465**, L15

- Wakker B. P., Hernandez A. K., French D. M., Kim T.-S., Oppenheimer B. D., Savage B. D., 2015, *ApJ*, 814, 40
- Werk J. K., Prochaska J. X., Thom C., Tumlinson J., Tripp T. M., O’Meara J. M., Peeples M. S., 2013, *ApJS*, 204, 17
- Wotta C. B., Lehner N., Howk J. C., O’Meara J. M., Prochaska J. X., 2016, *ApJ*, 831, 95
- York D. G., et al., 2000, *AJ*, 120, 1579
- Zabl J., et al., 2019, *MNRAS*, 485, 1961
- Zabl J., et al., 2021, *MNRAS*, 507, 4294
- Zibetti S., Ménard B., Nestor D. B., Quider A. M., Rao S. M., Turnshek D. A., 2007, *ApJ*, 658, 161
- van de Voort F., Schaye J., Booth C. M., Haas M. R., Dalla Vecchia C., 2011, *MNRAS*, 414, 2458
- van de Voort F., Schaye J., Altay G., Theuns T., 2012, *MNRAS*, 421, 2809

APPENDIX A: GALAXY PROPERTIES

Table A1 provides the galaxy details and measurements. In this table, we present the background quasar fields, galaxy ID, coordinates, and redshifts (z_{gal}). The galaxy–absorption projected distance (D), virial radius normalised impact parameter (D/R_{vir}), galaxy inclination angle (i), the angle between absorption and galaxy major axis (Φ), galaxy $g-r$ colour, stellar mass ($\log(M_*/M_\odot)$), and halo mass ($\log(M_{\text{h}}/M_\odot)$) are also presented in this table.

Table A1. Galaxy properties

Quasar	Galaxy	RA _{gal}	DEC _{gal}	z _{gal}	D (kpc)	D/R _{vir}	i (deg) ^a	Φ (deg) ^a	g − r	log(M _* /M _⊙) ^b	log(M _h /M _⊙)	References ^c
MRK335	NGC7817	00:03:58.91	+20:45:08.4	0.007702	343	2.41 ^{+0.08} _{−0.07}	80±1	87	0.87	10.43	11.75 ^{+0.1} _{−0.1}	2
J035128−142908	J0351G1	03:51:27.87	−14:28:57.9	0.356992	72.3±0.4	0.53 ^{+0.07} _{−0.07}	28.5 ^{+19.8} _{−12.5}	4.9 ⁺³³ _{−4.9}	0.29	10.05	11.55 ^{+0.1} _{−0.1}	1
PKS0405−123	PKS0405G1	04:07:45.63	−12:11:07.1	0.361102	233.7±0.4	0.72 ^{+0.36} _{−0.21}	44.6 ^{+2.4} _{−44.6}	4.4 ^{+1.9} _{−1.9}	0.45	11.06	12.67 ^{+0.4} _{−0.3}	1
J040748−121136	J0407G1	04:07:49.67	−12:11:05.5	0.495164	107.6±0.4	0.78 ^{+0.07} _{−0.07}	67.2 ^{+7.6} _{−7.5}	21.0 ^{+5.3} _{−3.7}	0.45	10.04	11.54 ^{+0.1} _{−0.1}	1
J045608−215909	J0456G1	04:56:08.93	−21:59:29.2	0.381511	103.4±0.3	0.6 ^{+0.1} _{−0.07}	57.1 ^{+19.9} _{−2.4}	63.8 ^{+4.3} _{−2.7}	0.45	10.49	11.86 ^{+0.12} _{−0.1}	1
J045608−215909	J0456G2	04:56:09.69	−21:59:03.9	0.277938	50.7±0.4	0.4 ^{+0.07} _{−0.07}	71.2 ^{+2.2} _{−2.6}	78.4 ^{+2.1} _{−2.0}	0.45	9.96	11.49 ^{+0.1} _{−0.1}	1
PG0804+761	UGC04238	08:11:36.77	+76:25:17.9	0.00515	148	1.56 ^{+0.06} _{−0.06}	75±10	62	0.45	9.59	11.21 ^{+0.1} _{−0.1}	2
J085334+434902	J0853G1	08:53:35.16	+43:48:27.3	0.09084	59.3±0.1	0.49 ^{+0.06} _{−0.06}	52.6 ^{+0.7} _{−0.9}	37.0 ^{+0.9} _{−1.2}	0.53	10.07	11.49 ^{+0.1} _{−0.1}	1
J085334+434902	J0853G2	08:53:45.24	+43:51:08.2	0.163403	26.2±0.1	0.18 ^{+0.08} _{−0.07}	70.1 ^{+1.4} _{−0.8}	56.0 ^{+0.8} _{−0.8}	0.45	10.37	11.70 ^{+0.1} _{−0.1}	1
SDSSJ091052+333008	NGC2770	09:09:33.71	+33:07:24.7	0.006498	239	1.81 ^{+0.07} _{−0.07}	80±5	63	0.58	10.29	11.64 ^{+0.1} _{−0.1}	2
TON1015	NGC2770	09:09:33.71	+33:07:24.7	0.006498	218	1.65 ^{+0.07} _{−0.07}	80±5	58	0.58	10.29	11.64 ^{+0.1} _{−0.1}	2
TON1009	NGC2770	09:09:33.71	+33:07:24.7	0.006498	267	2.03 ^{+0.07} _{−0.07}	80±5	38	0.58	10.29	11.64 ^{+0.1} _{−0.1}	2
FBQJ0908+3246	NGC2770	09:09:33.71	+33:07:24.7	0.006498	204	1.55 ^{+0.07} _{−0.07}	80±5	56	0.58	10.29	11.64 ^{+0.1} _{−0.1}	2
SDSSJ091127+325337	NGC2770	09:09:33.71	+33:07:24.7	0.006498	234	1.77 ^{+0.07} _{−0.07}	80±5	33	0.58	10.29	11.64 ^{+0.1} _{−0.1}	2
J091440+282330	J0914G1	09:14:41.76	+28:23:51.2	0.244312	105.9±0.1	0.81 ^{+0.07} _{−0.07}	39.0 ^{+0.4} _{−0.2}	18.2 ^{+1.1} _{−1.0}	0.17	10.04	11.54 ^{+0.1} _{−0.1}	1
J094331+053131	J0943G1	09:43:30.72	+05:31:17.5	0.353052	96.5±0.3	0.78 ^{+0.07} _{−0.07}	44.4 ^{+1.1} _{−1.2}	8.2 ^{+3.0} _{−5.0}	0.29	9.87	11.44 ^{+0.1} _{−0.1}	1
J094331+053131	J0943G2	09:43:32.31	+05:31:51.4	0.548494	150.9±0.6	0.88 ^{+0.09} _{−0.07}	58.8 ^{+0.6} _{−1.1}	67.2 ^{+0.9} _{−1.0}	0.25	10.44	11.82 ^{+0.11} _{−0.1}	1
J095000+483129	J0950G1	09:50:01.01	+48:31:02.3	0.211866	93.6±0.2	0.43 ^{+0.2} _{−0.12}	47.7 ^{+0.1} _{−0.1}	16.6 ^{+0.1} _{−0.1}	0.45	10.82	12.22 ^{+0.24} _{−0.17}	1
PG0953+414	PG0953G1	09:57:25.13	+41:20:22.5	0.058815	541.9±0.3	5.02 ^{+0.06} _{−0.06}	11.4 ^{+0.4} _{−0.2}	48.9 ^{+0.2} _{−0.2}	0.25	9.86	11.36 ^{+0.1} _{−0.1}	1
SDSSJ095914+320357	NGC3067	09:58:21.08	+32:22:11.6	0.004887	128	1.17 ^{+0.06} _{−0.06}	71±5	40	0.69	9.92	11.40 ^{+0.1} _{−0.1}	2
3C232	NGC3067	09:58:21.08	+32:22:11.6	0.004887	11	0.10 ^{+0.06} _{−0.06}	71±5	71	0.69	9.92	11.40 ^{+0.1} _{−0.1}	2
PG1001+291	PG1001G1	10:04:02.37	+28:55:12.3	0.137403	56.7	0.93 ^{+0.06} _{−0.07}	79.14 ^{+2.2} _{−2.1}	12.4 ^{+2.4} _{−2.9}	0.2	8.42	10.59 ^{+0.1} _{−0.1}	1
J100902+071343	J1009G1	10:09:02.74	+07:13:37.7	0.227855	64.0±0.8	0.44 ^{+0.08} _{−0.07}	66.3 ^{+0.6} _{−0.9}	89.6 ^{+0.4} _{−1.3}	0.45	10.26	11.68 ^{+0.1} _{−0.1}	1
RX_J1017.5+4702	NGC3198	10:19:54.95	+45:32:58.6	0.002202	370	2.90 ^{+0.07} _{−0.06}	73±2	58	0.56	10.24	11.60 ^{+0.1} _{−0.1}	2
J104116+061016	J1041G1	10:41:06.32	+06:09:13.5	0.442173	56.2±0.3	0.30 ^{+0.07} _{−0.06}	49.8 ^{+7.4} _{−5.2}	4.3 ^{+0.9} _{−1.0}	0.45	10.58	11.94 ^{+0.14} _{−0.11}	1
SDSSJ104335+115129	NGC3351	10:43:57.70	+11:42:13.7	0.002595	31	0.22 ^{+0.08} _{−0.07}	42±2	46	0.72	10.39	11.71 ^{+0.1} _{−0.1}	2
RX_J1054.2+3511	NGC3432	10:52:31.13	+36:37:07.6	0.002055	290	3.45 ^{+0.06} _{−0.06}	90±4	60	0.39	9.32	11.06 ^{+0.1} _{−0.1}	2
CSO295	NGC3432	10:52:31.13	+36:37:07.6	0.002055	20	0.24 ^{+0.06} _{−0.06}	90±2	79	0.39	9.32	11.06 ^{+0.1} _{−0.1}	2
PG1116+215	PG1116G1	11:19:06.70	+21:18:28.8	0.138114	138.0±0.2	0.76 ^{+0.14} _{−0.09}	26.4 ^{+0.8} _{−0.4}	34.4 ^{+0.4} _{−0.4}	0.45	10.69	12.00 ^{+0.17} _{−0.13}	1
PG1116+215	PG1116G2	11:19:18.07	+21:15:03.9	0.165916	814.4±0.7	4.17 ^{+0.17} _{−0.11}	49.5 ^{+0.2} _{−1.1}	47.2 ^{+1.8} _{−0.4}	0.45	10.75	12.08 ^{+0.21} _{−0.15}	1
RX_J1121.2+0326	NGC3633	11:20:26.22	+03:35:08.2	0.008629	184.0	1.25 ^{+0.09} _{−0.07}	72±5	55	0.87	10.45	11.80 ^{+0.11} _{−0.1}	2
RX_J1117.6+5301	NGC3631	11:21:02.87	+53:10:10.4	0.003856	78	0.82 ^{+0.06} _{−0.06}	17±5	78	0.51	9.62	11.22 ^{+0.1} _{−0.1}	2
SDSSJ112448+531818	NGC3631	11:21:02.87	+53:10:10.4	0.003856	86	0.90 ^{+0.06} _{−0.06}	17±5	77	0.51	9.62	11.22 ^{+0.1} _{−0.1}	2
SDSSJ11443+525834	NGC3631	11:21:02.87	+53:10:10.4	0.003856	145	1.52 ^{+0.06} _{−0.06}	17±5	74	0.51	9.62	11.22 ^{+0.1} _{−0.1}	2
SDSSJ112114+032546	CGCG039137	11:21:26.95	+03:26:41.7	0.023076	99	0.92 ^{+0.06} _{−0.06}	72±4	86	0.61	9.87	11.36 ^{+0.1} _{−0.1}	2
SDSSJ112439+113117	NGC3666	11:24:26.07	+11:20:32.0	0.003546	58	0.55 ^{+0.06} _{−0.06}	78±5	86	0.61	9.87	11.36 ^{+0.1} _{−0.1}	2
SDSSJ112448+531818	UGC06446	11:26:40.46	+53:44:48.0	0.002151	143	2.29 ^{+0.06} _{−0.07}	52±3	19	0.31	8.59	10.67 ^{+0.1} _{−0.1}	2
J113327+032719	J1133G1	11:33:28.27	+03:26:59.6	0.154598	55.6±0.1	0.52 ^{+0.06} _{−0.06}	23.5 ^{+0.4} _{−0.2}	56.1 ^{+1.7} _{−1.3}	0.2	9.78	11.31 ^{+0.1} _{−0.1}	1

Table A1. Galaxy Properties continued

Quasar	Galaxy	RA _{gal}	DEC _{gal}	z _{gal}	D (kpc)	D/R _{vir}	i (deg) ^a	Φ (deg) ^a	g - r	log(M _* /M _⊙) ^b	log(M _h /M _⊙)	References ^c
J113910-135043	J1139G1	11:39:05.90	-13:50:48.1	0.219724	127.1±0.1	1.38 ^{+0.07} _{-0.07}	7.1 ^{+20.1} _{-0.0}	22.7 ^{+4.5} _{-5.7}	0.45	9.23	11.09 ^{+0.1} _{-0.1}	1
J113910-135043	J1139G2	11:39:09.52	-13:51:31.8	0.212259	174.8±0.1	0.98 ^{+0.12} _{-0.08}	85.0 ^{+0.1} _{-0.6}	80.4 ^{+0.4} _{-0.5}	0.78	10.6	11.96 ^{+0.15} _{-0.11}	1
J113910-135043	J1139G3	11:39:10.01	-13:50:52.3	0.319255	73.3±0.4	0.47 ^{+0.08} _{-0.07}	83.4 ^{+1.4} _{-1.1}	39.1 ^{+1.9} _{-1.7}	0.45	10.34	11.74 ^{+0.1} _{-0.1}	1
J113910-135043	J1139G4	11:39:11.53	-13:51:08.6	0.204194	93.2±0.3	0.61 ^{+0.08} _{-0.07}	81.6 ^{+0.4} _{-0.5}	5.8 ^{+0.4} _{-0.5}	0.66	10.35	11.75 ^{+0.1} _{-0.1}	1
PG1216+069	PG1216G1	12:19:23.44	+06:38:20.1	0.123623	93.4	0.68 ^{+0.07} _{-0.07}	22.0 ^{+18.7} _{-21.8}	61.4 ⁺³³ _{-13.4}	0.41	10.29	11.64 ^{+0.1} _{-0.1}	1
MRK771	NGC4529	12:32:51.65	+20:11:00.6	0.008459	158	1.43 ^{+0.06} _{-0.06}	80±8	26	0.48	9.95	11.41 ^{+0.1} _{-0.1}	2
J123304-003134	J1233G1	12:33:03.76	-00:31:59.6	0.318757	88.9±0.2	0.55 ^{+0.09} _{-0.07}	38.7 ^{+1.6} _{-1.8}	17.0 ^{+2.0} _{-2.3}	0.45	10.40	11.78 ^{+0.11} _{-0.1}	1
SDSSJ123604+264135	NGC4565	12:36:20.78	+25:59:15.6	0.004103	147	0.76 ^{+0.19} _{-0.12}	86±7	38	0.85	10.79	12.15 ^{+0.23} _{-0.16}	2
J124154+572107	J1241G1	12:41:52.35	+57:20:53.6	0.205267	21.1±0.1	0.16 ^{+0.07} _{-0.07}	56.4 ^{+0.3} _{-0.5}	77.6 ^{+0.3} _{-0.4}	0.45	10.06	11.55 ^{+0.1} _{-0.1}	1
J124154+572107	J1241G2	12:41:52.49	+57:20:42.6	0.217904	94.6±0.2	0.82 ^{+0.07} _{-0.07}	17.4 ^{+1.4} _{-1.6}	63.0 ^{+1.8} _{-2.1}	0.29	9.77	11.38 ^{+0.1} _{-0.1}	1
PG1259+593	UGC08146	13:02:08.10	+58:42:04.7	0.002235	114	1.44 ^{+0.06} _{-0.06}	78±3	52	0.38	9.18	10.98 ^{+0.1} _{-0.1}	2
PG1302-102	NGC4939	13:04:14.39	-10:20:22.6	0.010317	254	1.35 ^{+0.17} _{-0.11}	61±4	64	0.57	10.76	12.10 ^{+0.21} _{-0.15}	2
J132222+464546	J1322G1	13:22:22.51	+46:45:46.0	0.214431	38.6±0.2	0.16 ^{+0.25} _{-0.14}	57.9 ^{+0.1} _{-0.2}	13.9 ^{+0.2} _{-0.2}	0.69	10.88	12.32 ^{+0.3} _{-0.2}	1
J134251-005345	J1342G1	13:42:51.76	-00:53:49.3	0.227042	35.3±0.2	0.16 ^{+0.22} _{-0.13}	0.1 ^{+0.6} _{-0.1}	13.2 ^{+0.5} _{-0.4}	0.45	10.84	12.26 ^{+0.26} _{-0.18}	1
QSO1500-4140	NGC5786	14:58:56.26	-42:00:48.1	0.009924	453	3.15 ^{+0.09} _{-0.07}	65±5	2	0.57	10.44	11.75 ^{+0.11} _{-0.1}	2
SDSSJ151237+012846	UGC09760	15:12:02.44	+01:41:55.5	0.006985	123	1.32 ^{+0.06} _{-0.06}	90±4	87	0.43	9.57	11.19 ^{+0.1} _{-0.1}	2
2E1530+1511	NGC5951	15:33:43.06	+15:00:26.2	0.005937	55	0.45 ^{+0.06} _{-0.06}	74±6	88	0.56	10.15	11.54 ^{+0.1} _{-0.1}	2
J154743+205216	J1547G1	15:47:45.70	+20:49:17.6	0.096499	79.8±0.5	1.13 ^{+0.06} _{-0.06}	80.9 ^{+1.8} _{-2.0}	54.7 ^{+2.0} _{-2.4}	0.45	8.82	10.79 ^{+0.1} _{-0.1}	1
J155504+362847	J1555G1	15:55:05.27	+36:28:48.1	0.189201	33.4±0.1	0.23 ^{+0.08} _{-0.07}	51.8 ^{+0.7} _{-0.7}	47.0 ^{+0.3} _{-0.8}	0.32	10.36	11.69 ^{+0.1} _{-0.1}	1
MRK876	NGC6140	16:20:58.16	+65:23:26.0	0.003035	113	1.48 ^{+0.06} _{-0.06}	49±4	18	0.43	9.09	10.93 ^{+0.1} _{-0.1}	2
H1821+643	H1821G1	18:21:54.53	+64:20:09.0	0.225111	116.6	0.97 ^{+0.07} _{-0.07}	32.9 ^{+0.04} _{-0.04}	17.5 ^{+0.4} _{-0.3}	0.62	9.86	11.44 ^{+0.1} _{-0.1}	1
J213135-120704	J2131G1	21:31:38.87	-12:06:44.1	0.43020	48.4±0.2	0.25 ^{+0.13} _{-0.09}	48.3 ^{+3.5} _{-3.7}	14.9 ⁺⁶ _{-4.9}	0.45	10.63	12.0 ^{+0.16} _{-0.12}	1
RBS1768	ESO343G014	21:37:45.18	-38:29:33.2	0.030484	466	3.96 ^{+0.06} _{-0.06}	90±5	75	0.57	10.06	11.48 ^{+0.1} _{-0.1}	2
J213745-143255	J2137G1	21:37:50.50	-14:30:03.2	0.075451	70.9±0.7	0.68 ^{+0.06} _{-0.06}	71.0 ^{+0.9} _{-1.0}	73.2 ^{+1.0} _{-0.5}	0.45	9.75	11.29 ^{+0.1} _{-0.1}	1
PHL1811	PHL1811G2	21:54:54.66	-09:23:25.39	0.325424	552.6±0.8	4.16 ^{+0.07} _{-0.07}	25.6 ^{+2.7} _{-4.5}	72.3 ^{+0.17} _{-0.72}	0.45	10.03	11.54 ^{+0.1} _{-0.1}	1
PHL1811	PHL1811G1	21:54:54.93	-09:23:31.1	0.176097	351.3±0.3	2.06 ^{+0.11} _{-0.08}	22.17 ^{+0.8} _{-0.3}	49.9 ^{+1.0} _{-1.0}	0.45	10.59	11.90 ^{+0.14} _{-0.11}	1
PHL1811	PHL1811G3	21:55:05.14	-09:24:25.9	0.157933	358.8±0.9	3.06 ^{+0.06} _{-0.06}	85.5 ^{+4.5} _{-0.5}	71.4 ^{+0.6} _{-0.7}	0.43	9.97	11.42 ^{+0.1} _{-0.1}	1
MRC2251-178	MCG0358009	22:53:40.85	-17:28:44.0	0.030071	355	2.21 ^{+0.11} _{-0.08}	61±4	74	0.63	10.58	11.89 ^{+0.14} _{-0.11}	2
J225357+160853	J2253G1	22:53:57.80	+16:09:05.5	0.153718	31.8±0.2	0.25 ^{+0.06} _{-0.06}	33.3 ^{+2.7} _{-2.0}	59.6 ^{+0.9} _{-1.8}	0.45	10.11	11.52 ^{+0.1} _{-0.1}	1
J225357+160853	J2253G2	22:54:00.37	+16:09:06.4	0.352787	203.2±0.5	1.61 ^{+0.07} _{-0.07}	36.7 ^{+6.9} _{-4.6}	88.7 ^{+1.3} _{-4.8}	0.08	9.90	11.46 ^{+0.1} _{-0.1}	1
J225357+160853	J2253G3	22:54:02.32	+16:09:33.4	0.390012	276.3±0.2	1.53 ^{+0.11} _{-0.08}	76.1 ^{+1.1} _{-1.2}	24.2 ^{+1.2} _{-1.2}	0.45	10.56	11.92 ^{+0.14} _{-0.11}	1
RBS2000	IC5325	23:28:43.43	-41:20:00.5	0.005043	314	2.81 ^{+0.06} _{-0.06}	25±4	67	0.57	9.98	11.43 ^{+0.1} _{-0.1}	2

^a We adopted the inclination angle errors from French & Wakker (2020), which were provided by David French (2024, private communication). We note that they used a 3 degree galaxy PA error, which we also adopt here.

^b We adopt a 0.1 dex error in the stellar masses given the scatter quoted in Bell et al. (2003). This error is propagated through to the halo mass errors and R_{vir} errors.

^c Galaxy kinematics measurements reference: (1) this work, (2) French & Wakker (2020).

APPENDIX B: QUASAR FIELD OBSERVATIONS

Here we present the quasar information and observations details. Table B1 includes nine columns and provides the QSO coordinates, redshift, COS observation proposal IDs, the grating(s) used for observation, photometry imager or survey, the filter used for imaging, and the *HST* imaging proposal ID.

APPENDIX C: ABSORPTION PROPERTIES

In Table C1, we present the measured properties of CGM H I absorption studied in this work. The absorbers are detected in the spectrum of the background quasar in each field presented in the first column of this table. The host galaxies and absorption redshifts can be found in the second and third columns, respectively. We present the rest-frame equivalent width of Ly α absorption, $W_r(1215)$, and its column density in columns 4 and 5, respectively. In column 4, there are five systems that Ly β is used to measure their EW co-rotation fraction as the Ly α is not covered by the QSO spectra (see table note). $f_{EW_{\text{corot}}}$ is presented in column 7 and the last column lists the source of the H I column density measurement.

This paper has been typeset from a $\text{\TeX}/\text{\LaTeX}$ file prepared by the author.

Table B1. QSO observations

Quasar	RA (J2000)	DEC (J2000)	z_{qso}	COS PID(s)	COS Gratings	Imager/Survey	Filter	HST PID
MRK335	00:06:19.5	+20:12:11.0	0.026	13814	G130M
J035128–142908	03:51:28.5	–14:29:08.7	0.616	13398	G130M, G160M	HST/WFPC2	F702W	5949
PKS0405–123	04:07:48.4	–12:11:36.7	0.573	11508	G130M, G160M	HST/WFPC2	F702W	5949
J040748–121136	04:07:48.4	–12:11:36.7	0.572	11541	G130M, G160M	HST/WFPC2	F702W	5949
J045608–215909	04:56:08.9	–21:59:09.4	0.533	12466,12252,13398	G160M	HST/WFPC2	F702W	5098
PG0804+761	08:10:58.7	+76:02:43.0	0.102	11686	G130M, G160M
J085334+434902	08:53:34.2	+43:49:02.3	0.514	13398	G130M, G160M	HST/WFPC2	F702W	5949
FBQSJ0908+3246	09:08:38.8	+32:46:20.0	0.26	14240	G130M
TON1009	09:09:06.2	+32:36:30.0	0.81	12603	G130M
TON1015	09:10:37.0	+33:29:24.0	0.354	14240	G130M
SDSSJ091052+333008	09:10:52.8	+33:30:08.0	0.116	14240	G130M
SDSSJ091127+325337	09:11:27.3	+32:53:37.0	0.29	14240	G130M
J091440+282330	09:14:40.4	+28:23:30.6	0.735	11598	G130M, G160M	HST/ACS	F814W	13024
J094331+053131	09:43:31.6	+05:31:31.5	0.564	11598	G130M, G160M	HST/ACS	F814W	13024
J095000+483129	09:50:00.7	+48:31:29.4	0.589	11598	G130M, G160M	HST/ACS	F814W	13024
PG0953+414	09:56:52.4	+41:15:22.1	0.234	12038	G130M, G160M	Pan-STARRS	<i>i</i>	...
3C232	09:58:20.9	+32:24:20.0	0.531	15826	G130M
SDSSJ095914+320357	09:59:14.8	+32:03:57.0	0.565	12603	G130M
PG1001+291	10:04:02.6	+28:55:35.2	0.329	12038	G130M, G160M	HST/WFPC2	F702W	5949
J100902+071343	10:09:02.1	+07:13:43.9	0.456	11598	G130M, G160M	HST/WFC3	F625W	11598
RX_J1017.5+4702	10:17:31.0	+47:02:25.0	0.335	13314	G130M
J104116+061016	10:41:17.2	+06:10:16.9	1.27	12252	G160M	HST/WFPC2	F702W	5984
SDSSJ104335+115129	10:43:35.9	+11:05:29.0	0.794	14071	G130M
CSO295	10:52:05.6	+36:40:40.0	0.609	14772	G130M
RX_J1054.2+3511	10:54:16.2	+35:11:24.0	0.203	14772	G130M
SDSSJ111443+525834	11:14:43.7	+52:58:34.0	0.079	14240	G130M
RX_J1117.6+5301	11:17:40.5	+53:01:51.0	0.159	14240	G130M
PG1116+215	11:19:08.6	+21:19:18.0	0.176	12038	G130M, G160M	HST/WFPC2	F606W	5849
SBS1116+523	11:19:47.9	+52:05:53.0	0.356	14240	G130M
SDSSJ112114+032546	11:21:14.0	+03:25:47.0	0.152	12248	G130M, G160M
SDSSJ112439+113117	11:24:39.4	+11:31:17.0	0.143	14071	G130M
SDSSJ112448+531818	11:24:48.3	+53:18:19.0	0.532	14240	G130M
J113327+032719	11:33:27.8	+03:27:19.2	0.524	11598	G130M, G160M	HST/ACS	F814W	13024
J113910–135043	11:39:10.7	–13:50:43.6	0.556	12275	G130M	HST/ACS	F702W	6619
PG1216+069	12:19:20.9	+06:38:38.5	0.331	12025	G130M, G160M	HST/WFPC2	F702W	...
MRK771	12:32:03.6	+20:09:30.0	0.063	12569	G130M
J123304–003134	12:33:04.0	–00:31:34.2	0.47	11598	G130M, G160M	HST/ACS	F814W	13024
SDSSJ123604+264135	12:36:04.0	+26:41:36.0	0.209	12248	G130M, G160M
J124154+572107	12:41:54.0	+57:21:07.4	0.583	11598	G130M, G160M	HST/ACS	F814W	13024
PG1259+593	13:01:12.9	+59:02:07.0	0.478	11541	G130M, G160M
PG1302–102	13:05:33.0	–10:33:19.0	0.278	12038	G130M, G160M
J132222+464546	13:22:22.7	+46:45:35.2	0.374	11598	G130M, G160M	HST/ACS	F814W	13024
J134251–005345	13:42:51.6	–00:53:45.3	0.326	11598	G130M, G160M	HST/ACS	F814W	13024
QSO1500–4140	15:03:34.0	–41:52:23.0	0.335	11659	G130M
SDSSJ151237+012846	15:12:37.2	+01:28:46.0	0.266	12603	G130M
RBS1503	15:29:07.5	+56:16:07.0	0.099	12276	G130M
2E1530+1511	15:33:14.3	+15:01:03.0	0.09	14071	G130M
J154743+205216	15:47:43.5	+20:52:16.6	0.264	13398	G130M, G160M	HST/WFPC2	F702W	5099
J155504+362847	15:55:04.4	+36:28:48.0	0.714	11598	G130M, G160M	HST/ACS	F814W	13024
MRK876	16:13:57.2	+65:43:11.0	0.129	11524	G130M
H1821+643	18:21:57.2	+64:20:36.2	0.297	12038	G130M, G160M	HST/ACS, Pan-STARRS	F814W, <i>i</i>	13024
J213135–120704	21:31:35.3	–12:07:04.8	0.501	13398	G160M	HST/WFPC2	F702W	5143
J213745–143255	21:37:45.2	–14:32:55.8	0.2	13398	G130M, G160M	HST/WFPC2	F702W	5343
RBS1768	21:38:49.9	–38:28:40.0	0.183	12936	G130M, G160M
PHL1811	21:55:01.5	–09:22:25.0	0.19	12038	G130M, G160M	Pan-STARRS	<i>i</i>	...
J225357+160853	22:53:57.7	+16:08:53.6	0.859	13398	G130M, G160M	HST/WFPC2	F702W	6619
MRC2251–178	22:54:05.9	–17:34:55.0	0.066	12029	G130M, G160M
RBS2000	23:24:44.7	–40:40:49.0	0.174	13448	G130M, G160M

Table C1. Absorption properties

Quasar	Galaxy	z_{abs}	$W_r(1215)$ (Å)	$\log(N(\text{H I})/\text{cm}^{-2})$	$f_{\text{EWcorot}}^{\text{b}}$	References ^c
MRK335	NGC7817	0.006936	0.424 ±0.028	13.32 ±0.03	0.15	1
J035128–142908	J0351G1	0.356706	1.198 ±0.018	16.86 ±0.03	0.69	2
PKS0405–123	PKS0405G1	0.360814	0.795 ±0.007	15.26 ±0.06	0.70	1
J040748–121136	J0407G1	0.495111	0.141 ±0.005 ^a	14.34 ±0.56	0.57	2
J045608–215909	J0456G1	0.381664	0.60 ±0.02	15.10 ±0.39	0.78	2
J045608–215909	J0456G2	0.27799	0.752 ±0.013	14.78 ±0.22	0.60	3
PG0804+761	UGC04238	0.005118	0.082 ±0.004	12.6 ±0.08	0.46	1
J085334+434902	J0853G1	0.090763	0.577 ±0.009	14.53 ±0.04	0.37	4
J085334+434902	J0853G2	0.163718	5.764 ±0.053	19.93 ±0.01	0.57	2
SDSSJ091052+333008	NGC2770	0.006115	0.363 ±0.061	13.22 ±0.11	0.07	1
TON1015	NGC2770	0.006064	0.334 ±0.033	13.24 ±0.08	0.15	1
TON1009	NGC2770	0.006597	0.338 ±0.023	13.38 ±0.12	0.29	1
FBQJ0908+3246	NGC2770	0.006467	0.345 ±0.056	13.81 ±0.05	0.58	1
SDSSJ091127+325337	NGC2770	0.00688	0.243 ±0.047	14.00 ±0.20	0.00	1
J091440+282330	J0914G1	0.244096	0.791 ±0.021	15.55 ±0.03	0.23	2
J094331+053131	J0943G1	0.354399	2.413 ±0.076	16.46 ±0.03	0.94	2
J094331.61+053131.4	J0943G2	0.548808	0.123 ±0.025 ^a	14.61 ±0.08	1.00	4
J095000+483129	J0950G1	0.211585	1.297 ±0.017	18.48 ±0.19	0.29	3
PG0953+414	PG0953G1	0.058755	0.27 ±0.01	13.96 ±0.07	0.68	5
SDSSJ095914+320357	NGC3067	0.004987	0.556 ±0.024	16.23 ±1.43	0.69	1
3C232	NGC3067	0.004805	6.63 ±0.09	20.09 ±0.02	0.52	1
PG1001+291	PG1001G1	0.137458	0.717 ±0.008	14.98 ±0.03	0.64	4
J100902+071343	J1009G1	0.227858	0.98 ±0.02	17.23 ±0.16	0.52	3
RX_J1017.5+4702	NGC3198	0.002079	0.057 ±0.019	13.18 ±0.12	1.00	1
J104116+061016	J1041G1	0.441546	1.146 ±0.027	18.19 ±0.14	0.94	3
SDSSJ104335+115129	NGC335	0.002341	0.762 ±0.068	14.53 ±0.12	0.85	1
RX_J1054.2+3511	NGC3432	0.002222	0.234 ±0.072	13.58 ±0.12	0.09	1
CSO295	NGC3432	0.002204	0.963 ±0.063	15.05 ±0.37	0.65	1
PG1116+215	PG1116G1	0.138513	0.516 ±0.004	16.20 ±0.03	0.59	5
PG1116+215	PG1116G2	0.166152	0.780 ±0.004	14.71 ±0.05	0.74	5
RX_J1121.2+0326	NGC3633	0.008934	0.19 ±0.08	13.70 ±0.18	0.00	1
RX_J1117.6+5301	NGC3631	0.003763	0.447 ±0.038	13.17 ±0.10	0.30	1
SDSSJ112448+531818	NGC3631	0.003701	0.241 ±0.052	13.18 ±0.11	0.75	1
SDSSJ11443+525834	NGC3631	0.003837	0.160 ±0.064	13.52 ±0.09	0.36	1
SDSSJ112114+032546	CGCG039137	0.023493	0.50 ±0.09	14.27 ±0.06	1.00	1
SDSSJ112439+113117	NGC3666	0.003487	0.664 ±0.044	15.53 ±0.67	0.61	1
SDSSJ112448+531818	UGC06446	0.002202	0.261 ±0.051	14.07 ±0.04	0.65	1
J113327+032719	J1133G1	0.154198	0.686 ±0.024	16.76 ±0.96	1.00	3
J113910–135043	J1139G1	0.219799	0.099 ±0.008 ^a	14.20 ±0.07	0.63	2
J113910–135043	J1139G2	0.212036	0.268 ±0.006 ^a	15.33 ±0.04	0.03	2
J113910–135043	J1139G3	0.319419	0.625 ±0.008 ^a	16.19 ±0.03	0.46	2
J113910–135043	J1139G4	0.204418	1.26 ±0.02	16.28 ±0.34	0.69	3
PG1216+069	PG1216G1	0.124006	1.417 ±0.008	[16.06,19]	0.17	5
MRK771	NGC4529	0.00849	0.229 ±0.012	13.03 ±0.49	0.39	1
J123304–003134	J1233G1	0.318659	0.964 ±0.024	15.72 ±0.02	0.43	2
SDSSJ123604+264135	NGC4565	0.003897	0.348 ±0.032	13.31 ±0.14	0.17	1
J124154+572107	J1241G1	0.205584	1.071 ±0.012	18.38 ±0.16	0.81	3
J124154+572107	J1241G2	0.218094	0.750 ±0.016	15.59 ±0.12	0.27	2
PG1259+593	UGC08146	0.002274	0.244 ±0.009	13.04 ±0.14	0.59	1
PG1302–102	NGC4939	0.011482	0.09 ±0.01	13.23 ±0.04	0.00	1
J132222+464546	J1322G1	0.214527	1.103 ±0.022	17.49 ±0.2	0.58	3
J134251–005345	J1342G1	0.227256	1.891 ±0.033	18.83 ±0.05	0.39	2
QSO1500–4140	NGC5786	0.010422	0.16 ±0.04	13.85 ±0.08	1.00	1
SDSSJ151237+012846	UGC09760	0.006804	0.44 ±0.07	14.50 ±0.15	0.10	1
2E1530+1511	NGC5951	0.006046	0.646 ±0.054	13.73 ±0.05	0.65	1
J154743+205216	J1547G1	0.096155	0.228 ±0.013	13.75 ±0.03	0.04	2

Table C1. Absorption Properties continued

Quasar	Galaxy	z_{abs}	$W_r(1215)$ (\AA)	$\log(N(\text{H I})/\text{cm}^{-2})$	$f_{\text{EWcorot}}^{\text{b}}$	References ^c
J155504+362847	J1555G1	0.189054	0.977 \pm 0.084	17.52 \pm 0.22	0.64	3
MRK876	NGC6140	0.00311	0.388 \pm 0.005	13.49 \pm 0.15	0.63	1
H1821+643	H1821G1	0.224874	1.03 \pm 0.02	15.55 \pm 0.02	0.32	5
J213135–120704	J2131G1	0.429825	3.189 \pm 0.038	19.88 \pm 0.10	0.58	2
RBS1768	ESO343G014	0.031304	0.51 \pm 0.01	13.05 \pm 0.08	0.00	1
J213745–143255	J2137G1	0.07532	0.279 \pm 0.007	13.96 \pm 0.02	0.86	2
PHL1811	PHL1811G2	0.323091	0.20 \pm 0.01	13.61 \pm 0.03	0.00	4
PHL1811	PHL1811G1	0.176514	0.470 \pm 0.003	14.93 \pm 0.03	0.98	5
PHL1811	PHL1811G3	0.157814	0.153 \pm 0.004	13.26 \pm 0.09	0.83	5
MRC2251–178	MCG0358009	0.030114	0.066 \pm 0.005	13.08 \pm 0.04	0.59	1
J225357+160853	J2253G1	0.153766	0.937 \pm 0.022	16.04 \pm 0.73	0.45	3
J225357+160853	J2253G2	0.352607	0.766 \pm 0.029	14.53 \pm 0.05	0.74	2
J225357+160853	J2253G3	0.390642	0.934 \pm 0.043	15.19 \pm 0.04	0.01	4
RBS2000	IC5325	0.005356	0.045 \pm 0.013	12.85 \pm 0.10	0.00	1

^a The rest-frame Ly β equivalent width is reported because the Ly α was not covered by the background QSO spectra. In these absorption systems the Ly β is used for the purpose of measuring the co-rotation fraction.

^b Uncertainties range between 0.001 – 0.008 as determined from a bootstrap analysis where we varied the galaxy and absorption redshifts within their error bars.

^c H I absorption column density reference: (1) [French & Wakker \(2020\)](#), (2) [Pointon et al. \(2019\)](#), (3) [Sameer et al. \(2024\)](#), (4) this work, (5) [Tripp et al. \(2008\)](#).